

Constraining GRB Emission Physics with Extensive Early-Time, Multiband Follow-up

A. Cucchiara^{1,2}, S. B. Cenko¹, J. S. Bloom¹, A. Melandri^{3,4}, A. Morgan¹, S. Kobayashi⁴, R. J. Smith⁴, D. A. Perley¹, W. Li¹, J. L. Hora⁵, R. L. da Silva^{2,9}, J. X. Prochaska², P. A. Milne⁶, N. R. Butler¹, B. Cobb⁷, G. Worseck², C. G. Mundell⁴, I. A. Steele⁴, A. V. Filippenko¹, M. Fumagalli², C. R. Klein¹, A. Stephens⁸, A. Bluck⁸, R. Mason⁸

acucchia@ucolick.org

ABSTRACT

Understanding the origin and diversity of emission processes responsible for Gamma-ray Bursts (GRBs) remains a pressing challenge. While prompt and contemporaneous panchromatic observations have the potential to test predictions of the internal-external shock model, extensive multiband imaging has been conducted for only a few GRBs. We present rich, early-time, multiband datasets for two *Swift* events, GRB 110205A and GRB 110213A. The former shows optical emission since the early stages of the prompt phase, followed by the steep rising in flux up to ~ 1000 s after the burst ($t^{-\alpha}$ with $\alpha = -6.13 \pm 0.75$). We discuss this feature in the context of the reverse-shock scenario and interpret the following single power-law decay as being forward-shock dominated. Polarization measurements, obtained with the RINGO2 instrument mounted on the Liverpool Telescope, also provide hints on the nature of the emitting ejecta. The latter event, instead, displays a very peculiar optical to near-infrared lightcurve, with two achromatic peaks. In this case, while the first peak is probably due to the onset of the afterglow, we interpret the second peak to be produced by newly injected material, signifying a late-time activity of the central engine.

Subject headings: gamma-ray burst: GRB 110205A, GRB 110213A - techniques: photometric, spectroscopic, polarimetric

1. Introduction

Despite the unassailable utility of GRBs as probes of the Universe (e.g. Tanvir et al. 2009; Totani et al. 2006; Salvaterra et al. 2009; Cucchiara et al. 2011), some basic questions about the nature of the emission mechanisms persist. The *internal-external* shock paradigm, whereby the prompt gamma rays arise from self-shocking of an unsteady relativistic wind (Kobayashi & Zhang 2003; Sari & Piran 1997) and the afterglow arises from shock interaction with the ambient medium (Zhang et al. 2003), has found support (e.g. Guidorzi et al. 2011; Shao & Dai 2005) and challenges (Zhang 2011) from observations. The role of the *reverse-shock* — that crossing back through the ejecta — in the dynam-

ics and observables remains largely unconstrained owing to the lack of good early time multicolor observations when the reverse-shock contribution should be most prominent. In the pre-*Swift* era only a handful of GRBs were detected with sufficient temporal resolution, but an unambiguous case of reverse-shock contribution was not established (Kobayashi 2000; Zhang et al. 2003; Gruber et al. 2011; Perley et al. 2008; Gomboc et al. 2008; Mundell et al. 2007a). The *Swift* satellite (Gehrels et al. 2004) has permitted unprecedented observations of GRBs at early times (Vestrand et al. 2006; Klotz et al. 2008), allowing rapid investigation of emission from hard X-ray to optical frequency regimes. Similarly, fast-response, robotic ground-based telescopes have been optimized in order to quickly follow-up *Swift* events. Thanks to

a trigger-rate of 100 events/year, a large variety of GRBs have been observed, showing several different characteristics. For example, afterglows have shown more transitional phases in their lightcurves than pre-*Swift* samples (Evans et al. 2009). In some cases, they show optical and X-ray flares, indicating a refreshing activity from the central engine (Falcone et al. 2007). All of this new information has made the quest of a “standard-model” very challenging, and, after six years of investigation, is still not fully understood.

In this paper we detail high-energy *Swift* observations of GRB 110205A and GRB 110213A, and associated ground based observations from several facilities typically starting around the end of the prompt emission. Multiband observations, spanning several orders of magnitude in frequency and time, in combination with afterglow spectroscopy and host galaxy imaging, represent two extensive datasets in order to further investigate the *reverse*-shock emission (see also Gao 2011). In §2 and §3 we present our datasets and the data analysis procedure; in §4 we show our light curves and spectral energy distribution modeling analysis, and the uncertainties involved in the theoretical modeling. Finally, §5 will summarize our finding and discuss some of the future prospects of GRB investigation. Throughout the paper all errors are quoted as a 90% confidence interval, unless otherwise noted. We use a standard cosmological model with $H_0 = 71$ km/s/Mpc, $\Omega_M = 0.27$, and $\Omega_\Lambda = 0.73$.

2. GRB 110205A Data Set

2.1. Space-based data

GRB 110205A was discovered by the *Swift* satellite on 2011 February 5 at $T_0 = 02:02:41$ (UT dates are used throughout this paper). The BAT instrument (Barthelmy et al. 2005) showed a complex structured emission in the 15 – 350 keV energy range (Beardmore et al. 2011a). The GRB lightcurve shows several overlapping peaks rising around $T_0 - 120$ s, with the tallest peak at $T_0 + 210$ s, and minor activity until $T_0 + 1500$ s. The duration of the main pulse, measured in the 15 – 350 keV energy range, was $T_{90} = 257 \pm 25$ s (Markwardt et al. 2011).

At the same time, the *Suzaku*-WAM all-sky monitor observed the emission from this object in

the 20 – 3000 keV energy range. Combined with the BAT data we constructed a joint spectrum in the energy range from 15 to 3000 keV, which is well fit by a power-law with exponential cutoff model ($dN/dE \sim E^{\Gamma_\gamma} \times e^{-(2+\Gamma_\gamma)E/E_{peak}}$). The best-fit spectral parameters are $\Gamma_\gamma = -1.59^{+0.07}_{-0.06}$ and $E_{peak} = 230^{+135}_{-65}$ keV. The energy fluence in the 15 – 3000 keV band calculated for this model is $2.7^{+0.7}_{-0.4} \times 10^{-5}$ erg cm $^{-2}$ (Sakamoto et al. 2011). Assuming this value and a redshift of $z = 2.22$ for GRB 110205A (see Sec 2.4) the isotropic-equivalent energy released is $E_{iso} = 4.34^{+0.4}_{-0.7} \times 10^{53}$ erg in 1 keV to 10 MeV range (Pal’Shin 2011).

The X-ray Telescope (XRT; Burrows et al. 2005) started observing the field 155.4 s after the trigger and showed an uncatalogued fading source at RA=10 h 58 m 31 s 13, Dec = +67 $^\circ$ 31’30 $''$ 8 (J2000), with an uncertainty of 1.5 $''$ (90% confidence, Beardmore et al. 2011b). The XRT and BAT data were obtained from publicly available repositories (Evans et al. 2007, 2009; Butler et al. 2007; Butler & Kocevski 2007). At early times ($T \lesssim 10^3$ s; note that henceforth, T is often used as a shorthand substitute for $T - T_0$), the lightcurve displays complex behavior, due probably to the temporal overlap of different pulses similar to the pulses identified in the BAT data, as well as flaring activity. After the prompt phase, the X-ray afterglow declines until ~ 600 s with a steep power law ($\alpha_X = 5.39 \pm 0.43$). Finally, the late-time behavior ($T \gtrsim 10^3$ s) can be fitted by a single power-law with decay index $\alpha_X = 1.65 \pm 0.05$. A double power-law with decay indices $\alpha_{X,1} = 1.67 \pm 0.05$ and $\alpha_{X,2} = 2.01 \pm 0.34$ and a possible break time around ≈ 80 ks after the GRB explosion provides a slightly better fit, but not statistically significant. Some flares are clearly visible throughout the X-ray lightcurve, likely indicating a continuation of the progenitor activity (see Figure 1), as previously seen in other GRBs (Falcone et al. 2007).

Using the early time data (“window-timing” mode), the XRT averaged spectrum can be fitted by an absorbed power-law model with photon index $\Gamma_X = 1.42 \pm 0.02$, while the late-time spectrum in the XRT energy bands can be fitted with an absorbed power-law with a photon spectral index of $\Gamma_X = 1.99^{+0.08}_{-0.07}$. In this case, the best fitted absorption column density, at $z = 2.22$, is $N_H = 3.5^{+1.6}_{-1.5} \times 10^{21}$ cm $^{-2}$, in addition to the Galactic value of 1.6×10^{20} cm $^{-2}$ (Kalberla et al.

2005).

Other space-based facilities provided additional high-energy coverage. The *Konus-Wind* experiment detected GRB 110205A in the 20–1200 keV energy range with a 4.5-sigma detection of a possible pre-cursor at $T_0 - 1360$ s. In addition, a soft tail up to $T_0 + 1200$ s has been detected, consistent with a similar detection by the Swift-BAT instrument. The total fluence is $S = 3.66 \pm 0.35 \times 10^{-5}$ erg cm $^{-2}$ in the 20-1200 keV range (Golenetskii et al. 2011b; Pal’Shin 2011).

Finally, 164 seconds after the BAT detection, the UVOT instrument (Roming et al. 2005) onboard *Swift* began observing GRB 110205A, identifying the source in the *white* band filter at RA=10^h58^m31^s.12 and Dec =+67°31’31[”].2 (J2000) with a 0[”].63 accuracy in both directions (Figure 2, Beardmore et al. 2011b). UVOT early time observations have been acquired in “image-event” mode, allowing a very detailed time-resolved analysis of the count rate variation in the UVOT detector. Using the HEASOFT tools UVOTEVTLC and UVOTMAGHIST we estimated the total flux inside a 5[”] region centered at the object position, while using an annular background region as suggested by Poole et al. (2008) and Breeveld et al. (2011). Data in the *white* filter were binned with a bin size of 8 s in order to reach a minimum signal-to-noise ratio (S/N) of 3 per bin, in particular during the prompt emission.

The afterglow was also detected in the *u*, *b*, *v* and *w1* filters up to $T = 8 \times 10^4$ s. The lack of detection in the other two, bluer, filters available on UVOT is consistent with the observed redshift.

2.2. Ground-based follow-up

Soon after the *Swift* trigger, several robotic facilities pointed at the GRB location providing a series of photometric observations from optical to near-infrared (NIR) and Radio bands. Our group first identified an infrared counterpart using the Peters Automated Infrared Imaging Telescope (PAIRITEL, Bloom et al. 2006) which consists of the 1.3 m Peters Telescope at Mt. Hopkins, AZ, formerly used for the Two Micron All Sky Survey (2MASS; Skrutskie et al. 2006), refurbished with the southern 2MASS camera. Observations began at 05:14:03, ~ 3.2 hr after the trigger, and continued until the source reached its hour-angle limit.

Further observations were obtained on the following day (Morgan et al. 2011; Morgan & Bloom 2011). The raw data files were processed using a standard IR reduction technique via PAIRITEL Pipeline III and resampled using SWarp¹⁰ (Bertin et al. 2002) to create 1.0[”]pixel $^{-1}$ images for final photometry.

The standard observing mode is to take three 7.8 s exposures in immediate succession at each dither position. These are then median-combined into 23.4-s “triplestacks,” which were subsequently binned iteratively until a large enough S/N was achieved at the source position for accurate photometry. Aperture photometry was performed using custom Python software, utilizing Source Extractor (SExtractor; Bertin & Arnouts 1996) as a back end. Eight calibration stars present in all images were chosen based on brightness, proximity of nearby contaminating sources, and location relative to bad pixels. The optimal aperture of 4[”] diameter was determined by minimizing the absolute error relative to 2MASS magnitudes of our calibration stars.

Calibration was performed by redetermining the zeropoint for each image individually by comparison to 2MASS magnitudes using these eight stars. The resulting statistical uncertainty in the zero-point is negligible relative to other sources of error. Additional, systematic sources of error are addressed in detail by Perley et al. (2010); we use a similar procedure here to determine the total uncertainty of each point.

We also observed the field of GRB 110205A with the automated Palomar 60 inch telescope (P60; Cenko et al. 2006) approximately 96 minutes after the *Swift*-BAT trigger time. After executing a series of pre-programmed *g*’, *r*’, *i*’, and *z*’ observations, we manually inserted deeper observations until the afterglow faded below our sensitivity threshold.

Basic processing (bias subtraction, flat-fielding, etc.) was performed by our custom IRAF¹¹ pipeline. Later images were stacked to increase sensitivity with the SWarp software. Instrumen-

¹⁰See <http://www.astromatic.net/software/swarp>.

¹¹IRAF is distributed by the National Optical Astronomy Observatory, which is operated by the Association for Research in Astronomy, Inc., under cooperative agreement with the National Science Foundation.

tal magnitudes were extracted using point-spread function (PSF) fitting routines from the IRAF DAOPHOT package, and were photometrically calibrated with respect to bright, nearby reference stars from the Sloan Digital Sky Survey (SDSS; Abazajian et al. 2009).

Multiband observations of the optical afterglow of GRB 110205A were also, acquired with the robotic 2-m Liverpool Telescope (LT) starting about 920 s after the trigger time. After taking a sequence of short exposures with the r' filter (6×10 s), the LT continued to monitor the field cycling through g' , r' , and i' filters, using increasing exposures times, until finishing about 155 min after the burst event. Two deeper, 300 s long, observations in the r' filter were acquired manually at the end of the night, when the OT was still clearly detected (see Figure 3). These observations were all photometrically calibrated using the same standard stars adopted for the Palomar data.

After ~ 4.5 days, when the afterglow faded beyond the detectability of these facilities, we activated our Target of Opportunity (ToO) program at the Gemini-North telescope (P.I. Cobb), in order to monitor the late time behavior of the optical transient and/or estimate the possible host galaxy contribution. We performed a series of 10x3 minutes exposure in r' and i' bands using the GMOS camera (Hook et al. 2004). We analyzed and coadded these datasets using the dedicated GEMINI tool included in the IRAF environment. Calibration was performed using calibration stars present in the P60 data and magnitude were estimated using Source Extractor. The afterglow was detected and its brightness in the two bands is consistent with the extrapolation from early-time data, following a single power-law behavior.

In order to establish a possible host galaxy contribution, we repeated our r' band observation on 11 March 2011. We collected a total exposure time of 40 minutes. No object is detected at a 3-sigma upper limit of $r' > 27.21$ mag, corresponding to a flux density limit of $4.88 \times 10^{-2} \mu\text{Jy}$, implying no significant host contamination in our earlier observations. A summary of all our observations can be found in Tables 4–14 and shown in Figure 3 with all our optical and infrared data.

The overall lightcurve in the optical and near-infrared bands after the first 300 s can be fitted

by a model with two double power-law components known as “Beuermann functions” (Beuermann et al. 1999):

$$F_i(t) = \sum_{n=1,2} F_{i,n} \left[\left(\frac{t}{t_{b_n}} \right)^{\alpha_n} + \left(\frac{t}{t_{b_n}} \right)^{\beta_n} \right]^{-1}.$$

The normalization factors ($F_{i,n}$) are different for each of the i datasets and are free parameters in our fitting procedure, as well as the power-law indexes (α_n and β_n) and the break times (t_{b_n}), which are considered to be the same for all the bands. In this formalism, the peaks of the individual function can be estimated as:

$$t_{peak,n} = t_{b_n} \times (-\alpha_n/\beta_n)^{1/(\beta_n-\alpha_n)}.$$

Both components are needed in order to account for the steep rise at early time and the exponential decay after the first peak at $t_{peak} = 985 \pm 48$ s. We fit our datasets simultaneously and the results are listed in Table 1 as well as presented in Figure 3, before correcting for Galactic extinction, $E(B - V) = 0.02$.

In addition, radio observations were performed with several facilities providing upper limits in the millimeter and sub-millimeter regimes (Zauderer et al. 2011a; Petitpas et al. 2011; van der Horst et al. 2011). The Expanded Very Large Array facility detected the radio afterglow 1.2 days after the burst, providing a flux density of $182 \pm 12 \mu\text{Jy}$ at a frequency of 22 GHz (Zauderer et al. 2011b).

2.3. Optical Polarization

Polarization observations were obtained with the RINGO2 polarimeter on the Liverpool Telescope. The procedure consists in observing the target object (GRB) and other seven stars in the field. Also, known unpolarized sources are observed the same night, in order to minimize the intrinsic polarization introduced by the polarimeter itself and to be able to detect any residual polarization in the GRB emission. A more detailed description of this procedure can be found in Guidorzi et al. (2006) and Steele et al. (2010). The first RINGO2 image was obtained starting at 02:06:43, 243 s after the BAT trigger time, during the brightening phase of the afterglow. The data

are consistent with the OT being unpolarized, but unfortunately, due to significant cloud cover we were able only to determine an upper limit of $< 16\%$ polarized (3-sigma confidence level).

A second observation, centered at 02:58:07.1, 56 min after the trigger, was performed under significantly better conditions. We measure the V -plus- R -band linear polarization of the OT as 3.6%, with a 2-sigma confidence interval of 0 - 6.2%. By randomizing the time sequence of values in the observed trace, we simulate an unpolarized data stream which has exactly the same photometric characteristics as our observations. From many such random realizations, we reject the unpolarized hypothesis at a confidence of 92%.

These values are consistent with the net optical linear polarization estimated in R band few hours after the burst at the level of $P \sim 1.4\%$, performed by the Calar Alto Observatory equipped with the CAFOS instrument (Gorosabel et al. 2011). Both observations are indicated as red and green arrows in Figure 3.

2.4. Absorption Spectroscopy

We began observing the optical afterglow of GRB 110205A with the FAST spectrograph (Fabricant et al. 1998) mounted on the 1.5m Tillinghast reflector at Mt. Hopkins Observatory at 5:11 on 2011 February 5. We obtained two 1800s spectra with the 300 line mm^{-1} grating, covering the wavelength range 3500–7500 Å (Cenko et al. 2011). The data were reduced using standard IRAF routines, including optimal extraction and wavelength calibration relative to a series of HeNeAr calibration lamps. Flux calibration was performed relative to the standard star Feige 34. The resulting coadded, normalized spectrum is shown in Figure 6.

Another spectrum (da Silva et al. 2011) was taken with the Kast spectrograph (Miller & Stone 1993) on the 3 m Shane reflector at Lick Observatory. The reduction procedure was the same as the previous one and the resolution of this spectrum is ~ 4 Å in the blue side (around 4500 Å) and ~ 10 Å in the red side (around 6500 Å). This spectrum shows a prominent damped Ly α (DLA) absorption system as observed in other GRBs. This feature, in combination with other metal lines (e.g. Fe II, Si II and Si II*, C IV) place

the GRB at $z = 2.21442 \pm 0.00044$ (Figure 7). Equivalent widths are estimated and listed in Table 2. The neutral hydrogen column density, estimated by fitting the DLA with a Voigt profile, is $\log(N_{\text{H}}) = 21.45 \pm 0.20$, consistent with the one derived by the X-ray analysis, likely implying minimum photoionization of the hydrogen in the circumburst material caused by the burst radiation field (Campana et al. 2010; Watson et al. 2007).

3. GRB 110213A Data Set

3.1. Space-based Data

GRB 110213A was discovered by *Swift* on February 13 at 05:17:29. The BAT lightcurve has a typical single-pulse shape, with $T_{90} = 48 \pm 16$ s, estimated in the 15–350 keV energy range. The time-averaged spectrum from $T_0 - 31.2$ to $T_0 + 32.8$ s is best fit by a simple power-law model with a power-law index of $\Gamma_{\gamma} = 1.83 \pm 0.12$. The fluence in the 15–150 keV band is $5.9 \pm 0.4 \times 10^{-6}$ erg cm^{-2} (D’Elia et al. 2011; Barthelmy et al. 2011; Stratta & D’Elia 2011). The *Konus-Wind* experiment also observed this event reporting similar results (Golenetskii et al. 2011a). Finally, the Gamma-ray Burst Monitor (GBM), onboard the *Fermi* satellite detected the prompt emission of this event (Foley 2011). In the energy range 50–300 keV, the spectrum is well fit by a power-law function with exponential cut-off. The power-law index is $\Gamma_{\gamma} = -1.44 \pm 0.05$ and $E_{\text{peak}} = 98.4_{-6.9}^{+8.6}$ keV. Using the observed fluence value of $1.03 \pm 0.03 \times 10^{-5}$ erg cm^{-2} and $z = 1.46$ (see §3.3) we derive an isotropic-equivalent energy of $E_{\text{iso}} = 7.2_{-0.08}^{+0.1} \times 10^{52}$ erg.

The *Swift* spacecraft slewed immediately, allowing the XRT to be on target in ~ 81 s and to continue observing up to ~ 50 ks after the GRB discovery. The XRT enhanced position of the afterglow is RA(J2000)=02^h51^m51^s.37, Dec(J2000)=+49°16′21″.2, with an uncertainty of 1.5 arcsec in both directions (Osborne et al. 2011). The XRT light curve can be modeled by different power-law components ($t^{-\alpha}$): initially, at $T < 200$ s, the afterglow steeply decays proportional to $\alpha = 4.96 \pm 0.21$. Subsequently, it flattens and then slowly rises as $\alpha = -0.44 \pm 0.10$ until $T \approx 1500$ s when it starts fading again with $\alpha = 1.08 \pm 0.04$. A final steepening occurs at $T \approx 10^4$ s, after which the X-ray decay as $\alpha = 1.98 \pm 0.04$. There

are hints of a possible jet break around ~ 1 day postburst, based on the last observation, which, if valid, would place useful constraints on geometry of the burst emitting region (Figure 10).

UVOT started observing ~ 100 seconds after the BAT trigger. The afterglow was detected in the *white, u, b, v* and *uvw1* filters at RA=02^h51^m51^s.40, Dec =+49°16'23".6, with an uncertainty of 0.61 arcsec in both directions (Figure 9). In contrast to the early X-ray data, no steep decay is detected at $T \lesssim 300$ s, and instead a rising behavior is present in the *white* band observations with a power-law index $\alpha = -2.08 \pm 0.23$. Similarly to GRB 110205A, two Beuermann functions fit our datasets simultaneously very well. A peak is detected at $T = 315 \pm 85$ s, after which the optical/UV emission fades as $\alpha = 1.10 \pm 0.24$ until a minimum flux point at around 2000 s, when the emission steeply brightens again with $\alpha = -2.02 \pm 0.34$. After reaching a second peak at $T \approx 4900$ seconds, the emission decays as $\alpha = 1.80 \pm 0.15$. Unfortunately, due to the afterglow faintness, the UVOT data are sparse, but still cover up to 50 ks after the burst.

3.2. Ground based follow-up

The Katzman Automatic Imaging Telescope (KAIT; Filippenko et al. 2001) responded to the trigger within ~ 70 s after the trigger, observing the afterglow in the unfiltered band followed by *V* and *I*. The data were analyzed similarly to the P60 data (§2.2) and calibrated using USNO cataloged field stars. The afterglow was detected until $T \approx 3000$ s, during the second rise seen in the UVOT data.

The P60 began observing the optical afterglow of GRB 110213A about 162 s after the trigger, and continued sampling the light curve beyond 10^5 s in the 4 optical filters available, complementing the KAIT observations and confirming the two-peak behavior of the low-energy afterglow emission.

Finally, in order to constrain the late-time ($T > 10^4$ s) behavior we triggered our ToO program at the Gemini-North telescope (P.I. Cobb), using the GMOS camera (Hook et al. 2004) in imaging mode, performing *r'* and *i'* observations six days after the trigger. The object brightness in these bands indicates a possible jet break, in agreement with the X-ray analysis, around $T \approx 1$ days after

the burst. A complete summary of our observations can be found in Tables 15–24, and the full light curve is shown in Figure 11 before correcting for Galactic extinction, $E(B - V) = 0.32$.

3.3. Absorption Spectroscopy

We also determined the redshift of this GRB with the Boller and Chivens Spectrograph mounted on the Steward 2.3-m Bok telescope on Kitt Peak, AZ. Based on several metal lines, including Fe II, Fe II*, Ni II and Al II, we found $z = 1.4607 \pm 0.0001$ (see Figure 12). Equivalent widths for some of these features are listed in Table 3.

4. Results

GRB 110205A and GRB 110213A present well-sampled light curves from high energy to optical and NIR bands, covering a large timeline. We now frame the observed behavior of the afterglow emission within the *internal-external* shock scenario, emphasizing the analogies and differences as well as the limitations of the current follow-up efforts. The data allow constraining statements about the emission mechanisms and the interaction of the afterglow with the surrounding material. Throughout the following we will use the usual notation where $F(\nu, t) \propto \nu^{-\beta} f(t)$, where $f(t)$ is a Beuermann function or a simple power-law model and β the spectral index.

4.1. GRB 110205A

GRB 110205A represents an important laboratory in which to test the standard *internal-external* shock model. It presents several characteristics of the “typical” GRB prompt emission as well as of the afterglow component. We can divide the detected emission into 3 main parts: 1) the prompt emission ($T \lesssim 400$ s), which has been observed by all three instruments onboard the *Swift* satellite; 2) the optical peak region ($400 \lesssim T \lesssim 10^3$ s after the burst); 3) the late time phase ($T \gtrsim 10^3$ s).

4.1.1. Prompt phase

The prompt emission of GRB 110205A, as detected by the BAT instrument, is composed of a series of peaks as seen in several other long GRBs.

The observed fluence, $f = 2.7_{-0.4}^{+0.7} \times 10^{-5}$ erg cm $^{-2}$, is on the higher end of the *Swift*-GRBs fluence distribution at similar redshift as estimated recently by Mészáros et al. (2011) and the isotropic energy emitted, E_{iso} , places GRB 110205A well within the 3-sigma confidence level of the $E_p - E_{iso}$ correlation for long GRBs (Amati et al. 2008).

Furthermore, similarly to other cases (e.g. GRB 080319B, Racusin et al. 2008), the XRT and UVOT instruments were able to begin observing before the end of the prompt phase. The multiple peak nature of the prompt emission is consistent with each peak being produced by internal shocks due to the collision of different shock fronts. In Figure 4 we overplot the UVOT *white* band lightcurve in comparison with the XRT and the BAT signal during the first 400 s after the burst trigger. A bright and very sharp peak at ~ 220 s ($\Delta t/t \lesssim 1$) is detected also in the UVOT band, and it is consistent with an internal dissipation process (Ioka et al. 2005).

Over the entire prompt phase, the X-ray and gamma-ray emissions have a similar average photon index ($\Gamma_{ave} \approx 1.59$) derived from the BAT and *Suzaku* data. Rescaling the hard X-ray emission into the XRT energy range, the lightcurves align with each other as can be seen clearly in Figure 1.

Furthermore, at the most prominent peak in the BAT data, at $T \sim 220$ seconds after burst, the X-ray spectral index is $\beta \sim -0.12 \pm 0.04$. In Figure 5 we present the spectral energy distribution (SED) constructed using the X-ray data and the *white* filter observation at $T = 220$ s. A single power-law extrapolation from the high-energy band overpredicts the *white*-band observation of a factor of ~ 2 , indicating that the X-ray and the optical emission may likely belong to the same segment of the SED and are produced by the same electron population (see also Rossi et al. 2011; Shen & Zhang 2009; Vestrand et al. 2006, for similar studies). The discrepancy in the observed low-energy flux is not surprising, since the broad band filter extends blueward at 2000 Å and redward up to 6000 Å. Part of the flux, then, is suppressed by the presence of the Lyman- α break which is redshifted at 3912 Å ($z = 2.214$).

A break between the X-ray and the optical bands (imposing ν^β with $\beta = 1/3$; dash-dotted line in the figure) would fit the data better, but would be inconsistent with the SED at later time.

In fact, as comparison, we present a multiband SED constructed at $T \approx 400$ s and $T \approx 520$ s after the burst. In these cases a break will be required in order to account for the change in the X-ray spectral index as seen in other similar cases (Rossi et al. 2011), probably due to one of the characteristic synchrotron frequencies. The following fast decline observed in the X-ray regime is probably due to the tail of the prompt emission and it is governed by the high-latitude effect (hereafter HLE, Kumar & Panaitescu 2000), for which emission from different viewing angles reach the observer with different delays due to light propagation effect (see Racusin et al. 2009, and references within for a complete taxonomy of the X-ray lightcurves). At the same time ($350 \lesssim T \lesssim 600$), the X-ray spectrum undergoes a hard-to-soft evolution which has been characteristic of a large number of GRBs. In the HLE, the temporal and spectral indices are correlated such that $\alpha = 2 + \beta$ (Kumar & Panaitescu 2000). In the case of GRB 110205A, this is not satisfied because the derived values are $\alpha_X = 5.39$ and $\beta_X \approx 0.5$, but, as shown in Zhang et al. (2006), shifting the time zero point (t_0) of the afterglow can reconcile the the observation with the theory without ruling-out the curvature-effect interpretation. Assuming that the afterglow starts at $t_0 \approx 200$ s a new fit of the X-ray light curve gives a temporal index of $\alpha_X = 2.70 \pm 0.10$, in agreement with the expected value from the curvature effect ($\alpha_{theo} = 2.5$).

4.1.2. Optical peak time

After 600 seconds, the X-ray afterglow declines with a temporal index $\alpha_X = 1.65$, likely the signature of a *forward*-shock dominated emission taking place. Flaring activity is also detected at this time, which is not unusual for the X-ray emission (Margutti et al. 2011; Chincarini et al. 2010; Gao 2009; Marshall et al. 2011).

At the same time, however, the optical emission undergoes a steep increase in flux: assuming that this rising begun at the time of the trigger ($t_0 = t_{trigger}$) the optical flux increases as $t^{-\alpha_{opt}}$, with $\alpha_{opt} = -6.13 \pm 0.75$ ($\chi^2/d.o.f. = 1.29$) until $t_{peak} \approx 985$ s. As discussed in other cases (Liang et al. 2006; Quimby et al. 2006; Lazzati & Begelman 2006; Kobayashi et al. 2007; Rossi et al. 2011) the power-law index is very sensitive to the choice of t_0 . In particular, the rise slope is estimated

by $d \ln F_\nu(t)/d \ln(t - t'_0)$, where $t'_0 = t_{\text{trigger}} + t'$, instead of the usual $d \ln F_\nu(t)/d \ln(t - t_{\text{trigger}})$. Assuming that the optical emission started *after* the actual trigger time ($t' > 0$), for example at the time of the optical brightest point in the *white* band (see previous section), the fit slightly improves ($\chi^2/\text{d.o.f.} = 1.19$) and a shallower rising index of $\alpha_{\text{opt}} = -3.96 \pm 0.86$ is obtained. This value is consistent with a reverse-shock theoretical prediction (e.g., $\alpha_{\text{theo}} = -5$; Zhang et al. 2003). Instead, assuming an *earlier* emission ($t' < 0$) does not produce a better fit and, as result, implies an even steeper power-law index. In this last scenario, considering also the absence of a clear precursor in the gamma-ray band, it would be difficult to explain such emission in the optical before the hard X-ray.

Overall, this peculiar behavior, similar in all the observed bands from UV to Optical, can originate from a *forward*-shock or, as suggested in a few other cases, from the *reverse*-shock. In both cases, assuming the synchrotron self-absorption frequency is well below the optical band, $\nu_a < \nu_{\text{opt}}$, the thickness of the shell and the density profile (“homogenous ISM” [interstellar medium] or “wind-like” medium) affect the rate at which the lightcurve rises.

For instance, we are aware of no theoretical model that predicts such steep rising during the forward-shock, while if the rising is due to the onset of the afterglow it is important to determine if we are in the “thin-shell” or “thick-shell” regime (e.g. Kobayashi 2000; Sari et al. 1998). For a “thin-shell”, in a constant ISM, the temporal index is either $\alpha = -2$ ($\nu_c < \nu_{\text{opt}}$) or $\alpha = -3$ ($\nu_c > \nu_{\text{opt}}$, Zhang et al. (2003)). A “thick-shell” would imply a much shallower rise in flux before the peak. In case of a wind-like medium we expect a much shallower rise ($\alpha = -1/2$, Kobayashi & Zhang (2003)). Therefore is very unlikely that either a forward-shock emission or the passage of a synchrotron characteristic frequency in the observed band could reproduce the observed early-time optical lightcurve.

A reverse-shock can produce the observed rising, but again it is critical to determine the regime in which the emission takes place (Zhang et al. 2003). First of all, the $\alpha \approx -5$ can be only exist in a thin-shell regime, since the thick regime has a shallower rising $\alpha = -1/2$. We define

$\mathfrak{R}_\nu = \frac{\nu_R}{\nu_{m,r}(t)}$, the ratio between the optical R band frequency and the typical synchrotron frequency ν_m . For the reverse shock, $\mathfrak{R}_\nu > 1$ ($\nu_{m,r} < \nu_R$, thin shell, reverse-shock). We can calculate $\nu_{m,r}$ and $\nu_{c,r}$ at the peak, 985 s after the burst, since we expect $\nu_{c,r}(t_{\text{peak}}) = \nu_{c,f}(t_{\text{peak}})$, where the subscripts indicate the reverse and forward shock respectively. From Eq. 1 of Zhang et al. (2003), we obtained that the critical Lorentz factor is $\gamma_c \approx 550$, while the initial Lorentz factor can be estimated from the Lorentz factor at the peak time, γ_{peak} (Mészáros 2006):

$$\gamma_0 = 2 \times \gamma_{\text{peak}} = 2 \times \left(\frac{3(1+z)^3 E}{32\pi n m_p c^5 t_p^3} \right)^{1/8} \approx 200 \left(\frac{E}{4 \times 10^{53} \text{ erg}} \right)^{1/8} n^{-1/8} \left(\frac{1+z}{3.22} \right)^{3/8} \left(\frac{t_p}{985 \text{ s}} \right)^{-3/8}.$$

For GRB 110205A we see that $\gamma_0 < \gamma_c$, confirming that our assumption of thin shell regime is indeed correct. At the time of the peak: $\nu_{c,r} = 2.31 \times 10^{16} \text{ Hz}$ (for $\epsilon_B = 10^{-2}$) and $\nu_{m,f} = 1.2 \times 10^{15}$. Finally, using $\nu_{m,r} \sim \gamma_0^{-2} \nu_{m,f}$ we can see that we are likely in $\nu_{m,r} < \nu_R < \nu_c \lesssim \nu_X$. Another point in favor of a thin-shell regime is the burst duration. In fact, in this case the deceleration time t_γ is longer than the duration of the burst T_{90} , while for a thick-shell we would expect a much shorter time-scale.

If the optical band is located below the typical frequency of the *forward*-shock at the deceleration time ($\nu_{\text{opt}} < \nu_{m,f}$), the optical band pass is dominated by the *reverse*-shock emission. Although this interpretation seems favorable in explaining the temporal behavior, in this scenario the lightcurve should manifest the passage of $\nu_{m,f}$ in the observed bands (see Fig. 1 in Kobayashi & Zhang 2003), and it is not consistent with the observations. Then, the optical band should be roughly around or above $\nu_{m,f}$ at the deceleration time. We can estimate this from

$$\nu_{m,f} = (6 \times 10^{15} \text{ Hz})(1+z)^{1/2} E_{52}^{1/2} \epsilon_e^2 \epsilon_B^{1/2} (t/1 \text{ day})^{-3/2}.$$

Which, for the observed value of E_{iso} , z , and time of the peak, and using typical values for ϵ_e and ϵ_B , we estimate $\nu_{m,f} \approx 3 \times 10^{14} \text{ Hz}$. Under this condition, the onset of the afterglow is expected to be a single peak as observed in other cases (Mundell et al. 2007a,b). At the peak time,

the contributions of the two shock emissions to the optical band are comparable, provided that the microscopic parameters are similar in the two shocked regions. The rapid rise is due to the bright reverse shock emission which masks the onset of the forward-shock emission, and it implies a weakly magnetized outflow from the central engine (Fan et al. 2002; Zhang et al. 2003; Kumar & Panaitescu 2003; Gomboc et al. 2008).

It is worthwhile to note that the peak flux density in V band is 3 mJy, as observed by UVOT, and it is consistent with the sample of Panaitescu & Vestrand (2011) (see also Vestrand et al. 2006) for “peaky” afterglows, where, for a constant-ISM model and after a steep rise due to the fireball deceleration, the optical emission reaches a flux density of ~ 4 mJy (see Figure 8). After the onset of deceleration the afterglow is forward-shock dominated and evolves with the usual single power-law decay (except for the presence of a possible jet-break).

4.1.3. Late-time behavior

After the reverse shock has passed through the GRB ejecta, the synchrotron emission produced by an external shock interacting with the ISM becomes the dominant emission mechanism. The emission from the reverse shock decays as fast as t^{-2} , so we expect a power-law decline as $t^{-\alpha}$, with $\alpha = (3p - 2)/4$ (for $\nu_{opt} < \nu_c$) or $\alpha = 3(p - 1)/4$ (for $\nu_m < \nu_{opt} < \nu_c$). The late time optical-NIR decay indexes are $\alpha_{opt} = 1.74 \pm 0.28$, in agreement with the X-ray decay index $\alpha_X = 1.65 \pm 0.05$, suggesting a forward shock producing the emission from the optical to the X-ray. Assuming that the X-ray afterglow emission is dominated by forward shock, we estimated $p = 2.90$ ($\alpha_X = (3p - 2)/4$), where p is the index of the power-law distribution of random electrons accelerated at the shock (Zhang et al. 2003).

The observations performed by the RINGO2 polarimeter exclude the zero-polarization hypothesis at 92% confidence level, supporting the reverse plus forward shock scenario, in which the afterglow is mainly dominated by the forward shock. Nevertheless such low polarization as $P = 3.6\%$ can be the result of several scenarios, like a structured jet (Rossi et al. 2004), the alignment of the magnetic field over causally connected regions (Gruzinov & Waxman 1999), or even a large scale

magnetic fields in the ambient medium (Granot & Königl 2003). This result is also consistent with many other GRB polarization measurements (see Covino et al. 2004; Mundell et al. 2010, and references therein for the state of the art of polarization studies).

4.1.4. Absorption Spectrum

We also observed the afterglow of GRB 110205A with the Kast spectrograph on the 3 m Shane reflector at Lick Observatory. Despite the fact that only a few absorption features could be identified, a clear indication of high neutral hydrogen in the host galaxy of this GRB comes from the detection of a DLA absorption system. A fit of the broad absorption profile indicates a value of $\log(N_H/\text{cm}^{-2}) = 21.45 \pm 0.2$ (Figure 7), similar to the value obtained from the X-ray data, perhaps indicating minimal photoionization of the surrounding medium from the GRB itself (see also Campana et al. 2010; Watson et al. 2007).

4.2. GRB 110213A

Optical data for GRB 110213A were obtained only after the prompt emission had ended. Nevertheless, our group was able to observe this event from several different facilities, such as the P60 and KAIT, providing much coverage of the afterglow phase.

4.2.1. Prompt phase

The prompt emission exhibits a single-peak profile and a soft spectrum. Using E_{peak} and E_{iso} derived by *Swift* and other space facilities, GRB 110213A does not differ from other long-soft GRBs; thus, not surprisingly, it also obeys the Amati relation for long GRBs (Amati et al. 2008).

4.2.2. X-ray lightcurve

In the time between the beginning of the observations with XRT/UVOT and KAIT, the X-ray fades steeply with $\alpha_X = 4.96 \pm 0.21$. This early steep declining phase, as for GRB 110205A, is consistent to be the tail of the prompt emission and it is governed by the curvature effect. In particular, the spectral index and the temporal index are correlated by $\alpha = 2 + \beta$. Using the estimated photon index from the first 150 s ($\Gamma_X = 5.10 \pm 0.78$), we

obtain $\alpha = 6.10 \pm 0.78$, which is consistent with the observed steep decay at a $1\text{-}\sigma$ confident level. At $T > 150$ s the X-ray emission brightens with $\alpha_X = -0.44 \pm 0.10$ up to ~ 1500 s and then follows a shallow decay until 10^4 s with $\alpha_X = 1.08 \pm 0.04$.

Using the spectral index $\beta_X = 1.12 \pm 0.12$ we can determine that the behavior of GRB 110213A is consistent with the forward-shock scenario where the central engine is ejecting material in a slow-cooling regime in a homogenous ISM. Using the closure relation $\alpha = (q - 2)/2 + (2 + q)\beta/2$ we obtain $\alpha = -0.44$, where q is defined as $q = 2(\alpha + 1 - \beta)/(1 + \beta)$, for $\nu > \nu_c, \nu_m$ and characterizes the central engine behavior (where we have $q < 1$ for an adiabatic fireball modified by continued injection as presented in Zhang et al. 2006). The peak represents the cessation of the energy injection, after which the normal adiabatic expansion of the fireball is expected. We derive for $10^4 \lesssim t \lesssim 10^6$ s a decay index of $\alpha_X = 1.98 \pm 0.07$. In summary, the overall X-ray behavior of GRB 110213A is consistent with that of other GRBs in the *Swift* sample (e.g. Evans et al. 2009).

4.2.3. Optical behavior - $T < 2000$ s

KAIT observations of GRB 110213A indicate a rising afterglow with $\alpha = -2.08 \pm 0.23$ from $T = 70$ s until $T = 321$ s. From the sample of Oates et al. (2011, 2009), UVOT observed 6 GRBs with rising afterglows in the first 500 s. GRB 110213A has a very similar case. What can be the cause of the peak at 321 s? Several possibilities need to be tested: 1) the passage of one of the characteristic frequencies (e.g. ν_m); 2) a reverse shock, as seen in GRB 110205A; 3) a decreasing extinction with time; 4) the onset of the forward shock.

The characteristic frequency ν_m that produces a peak in the lightcurve has a time dependence of $\nu_{m,f} \propto t^{-3/2}$ and should produce a chromatic break, meaning that the peak should be earlier in the bluer bands than the redder ones. During the rising part only KAIT, UVOT *white* and P60 r' band observations are available, so it is a challenging task to assess this chromaticity due to the gaps in the light curve. Nevertheless, during the passage of ν_m the spectral index changes from $\nu^{1/3}$ (for $\nu < \nu_m$) to $\nu^{-(p-1)/2}$ (for $\nu_m < \nu < \nu_c$). Based on this we can estimate that the color change between the UVOT *white* filter and P60 r' observation before and after the peak should

be 0.68 mag. Instead, we measure a color difference of 0.15 ± 0.10 (after correcting for Galactic extinction). Furthermore, if we assume a constant density medium, $\nu_{m,f}$ can be calculated as:

$$\nu_{m,f} = (6 \times 10^{15} \text{ Hz})(1+z)^{1/2} E_{52}^{1/2} \epsilon_e^2 \epsilon_B^{1/2} (t/1 \text{ day})^{-3/2}.$$

For $z = 1.46$, $E_{52} = 7.2$ and $t = 0.004$ day, and assuming that $\nu_{m,f}$ is already below the r' band we obtain the constraint $\epsilon_e^2 \epsilon_B^{1/2} < 5.6 \times 10^{-6}$, consistent with other GRBs in the samples of Oates et al. (2009) and Panaitescu & Kumar (2002), in which the values of $\epsilon_e^2 \epsilon_B^{1/2}$ range from 3×10^{-3} and 2×10^{-7} . Therefore we can exclude that the peak observed is due to the passage of ν_m . As suggested by some authors (Klotz et al. 2008; Rykoff et al. 2004), if there were a significant amount of extinction at the beginning of the afterglow phase the resulting light curve would be dim and reddened. Then, because of dust-destruction effect, it would rise faster in the blue filters than in the red ones. Of course this effect strongly depends on the GRB environment, but the KAIT, P60 and UVOT white observations, which all trace the rising phase, show similar α index, from the blue bands (UVOT *white*) to the red (P60 r'). So we can also exclude that this effect is the dominant cause of the rising at early time.

The rising in the light curve at $T < 321$ s is more likely due to the onset of the forward shock. Unlike GRB 110205A, the rather slow rise does not require the domination of the reverse-shock emission at early times. The post-peak decay $\alpha = 1.10 \pm 0.24$ is also much shallower than the typical reverse-shock index ($\alpha = 2$). The forward-shock emission masks the reverse-shock emission when the typical frequency of the forward shock is below the optical band or when the magnetization of the ejecta is very high ($\sigma = B^2/4\pi\gamma\rho c^2$ is about unity or larger) and the magnetic pressure suppresses the reverse-shock emission (Giannios et al. 2008). The observed $\alpha = -2.08$ is consistent with the expected $\alpha = -2$ for $\nu_c < \nu_{\text{opt}}$, in a ‘‘thin’’-shell scenario for a homogeneous ISM.

Finally, for a constant density medium, we can use the peak time to determine the Lorentz factor at that time using the formalism of Sari & Piran (1999), like in similar other cases Molinari et al. (2007). We obtain $\Gamma(t_{\text{peak}}) \approx 139(\eta n_0)^{-1/8}$,

where η and n_0 are the radiative efficiency and the density of the shocked medium respectively. Usually the initial Lorentz factor is twice the value at peak, allowing us to estimate the deceleration radius of the fireball to be $R_{dec} \approx 2.27 \times 10^{17}$ cm. The Lorentz factor and the deceleration radius are also consistent with the theoretical values predicted by Rees & Meszaros (1992), as well as with the sample of Oates et al. (2009).

4.2.4. Optical behavior - $T > 2000$ s

A second peak at $t_{peak} = 4975 \pm 545$ s is detected by several facilities, but is most prominent in data from the Palomar P60 and, in the decaying phase, the UVOT. Again, as previously, this feature can be due to one of the characteristic frequencies passing in the optical bands (in particular, at such late time, the synchrotron characteristic frequency ν_c). Another possibility is that the emission is from the newly injected material in the blastwave (energy injection model).

In the case of synchrotron origin we calculated the optical spectral indices before and after the peak at $t_{peak} = 4975$ s. We obtain $\beta_{o,pre} = 1.12 \pm 0.24$ and $\beta_{o,post} = 1.22 \pm 0.18$. These values are consistent with each other within $1-\sigma$, indicating that $\nu_c < \nu_{z'}$ or $\nu_c > \nu_{white}$ at $t = t_{peak}$.

Also, the passage of a characteristic frequency during our observation would imply a chromatic feature, mainly a different peak time at different frequencies. We tested this possibility assuming, for example, that the peak in z' band at $t_{z',p} = 4975$ s is due to the characteristic synchrotron frequency. Using the scaling law in Sari et al. (1998), we estimated that the peak would have crossed the UVOT u band at:

$$t_{u,p} = t_{z',p} \times \left(\frac{\nu_{c,z'}}{\nu_{c,u}}\right)^2 = 743 \text{ s.}$$

From Figure 11 it is evident that this is not the case.

One more possibility which would produce a ‘‘bump’’ in the lightcurve is the interaction of the fireball with moderate overdensity regions in the ambient medium (Lazzati et al. 2002). Although, in this case, the lightcurve returns to the original power-law decay after the fireball has passed through these overdensity regions, which is inconsistent with our observations.

Instead, the most likely scenario, in agreement with the X-ray analysis, is that the rise and the following decays at late time are due to the re-injected material from the central engine into the ISM. At late time, in this case, we expect a somewhat steeper decay than the usual adiabatic regime ($\alpha = (2 - 3p)/4$). The decay index from the optical multiband fit is consistent with $\alpha = 1.80 \pm 0.15$, in agreement with the X-ray emission, whereas the adiabatic regime gives $\alpha = 1.37$ assuming a typical value of $p = 2.5$. Our assumption of a reinjection phase better explains our late-time data.

Finally, using our Gemini ToO program we observed the afterglow in the r' and i' bands around 6 days after the burst. The object is detected, but significantly below the extrapolation of the light curve from the early data. This suggests the presence of a jet break after 1 day, placing a constraint on the opening angle of $\theta_{jet} \gtrsim 5^\circ$, and assuming the afterglow is the dominant source of radiation with a negligible contribution from the host galaxy.

4.2.5. Absorption Spectrum

The redshift of $z = 1.46$, determined using the Bok telescope allows the identification of UV rest-frame lines of low-ionization species. In particular, fine-structure transitions, like Ni II* and Fe II*, are indicative of UV pumping as the principle excitation mechanism in the vicinity of the GRB. No neutral hydrogen estimate is possible, again, due to the low-redshift nature of this GRB.

5. Conclusion

We observed GRB 110205A and GRB 110213A, discovered by the *Swift* satellite, with a broad range of follow-up facilities. The combination of our datasets and the publicly available *Swift* data covers more than six orders of magnitude in time.

GRB 110205A represents one of the best cases in which it has been possible to determine the contribution of the *reverse*-shock. While the UVOT and XRT data trace very well the prompt phase, they also allow the characterization of a fast rising ($\alpha = -6.13 \pm 0.75$) due to the reverse shock. After the peak at $T \approx 985$ s, the behavior is consistent with a combination of reverse and forward shocks, providing a shallower decay than the

one expected for a pure *reverse*-shock. A polarization measurement around 9 minutes after the burst provides only an upper limit (limiting polarization of $< 16\%$), with a 2-sigma linear polarization detection obtained around one hour post-burst ($P = 3.6\%$). This value, is in agreement with other estimates ($P = 1.4\%$, Gorosabel et al. 2011). Unfortunately, in the absence of polarization variability information, we were unable to constrain the nature of the GRB environment or of the jet. Nevertheless, the reverse shock emission dominates over the optical band and masks the forward shock emission at early times and it implies a weakly magnetized fireball.

Ground-based optical spectra reveal the presence of a strong DLA absorption system at $z = 2.22$, produced by a neutral hydrogen column density of $\log(N_{\text{H}}/\text{cm}^{-2}) = 21.45 \pm 0.2$. This is not surprising, but it is interestingly similar to the value obtained from the X-ray data, implying minimal photoionization of the surrounding medium from the GRB itself.

In contrast, GRB 110213A presents a clear indication of a refreshed shock, most likely produced by long-lived activity of the central engine. In the X-ray, the plateau phase is followed by the typical adiabatic behavior and by a steep decaying phase consistent with post-injection emission. In the optical, using 7 bands (from the UVOT-*white* to the P60 z' filters), the afterglow presents two peaks due to the onset of the forward shock and to the interaction of the injected material with the ISM. Other interpretations, such as the passage of the characteristic synchrotron frequencies in the observed bands, are ruled out since no chromatic features are present in our datasets. In the case of GRB 110213A, then, the forward-shock emission masks the reverse-shock emission, which means that the typical frequency of the forward shock is lower than the optical band or that the magnetic pressure is suppressing the reverse shock.

Using our late time Gemini observations we were also able to detect the afterglow well beyond the capabilities of our small robotic telescopes. These observations provide some constraints on the jet opening angle of the GRB emission. In particular we can place a lower limit of $\theta_{\text{jet}} \gtrsim 5^\circ$.

The importance of robotic facilities, multiband observations, and spectroscopic follow-up reinforces the notion that a large array of facilities

are needed in short order to interpret the complex early-time behavior of GRBs. Future implementations, in particular using near-infrared cameras mounted on larger facilities, will allow the characterization of even higher redshift events, and will help test the dust properties of their environments (e.g. Farah et al. 2010). The synergy between ground-based and new-generation space-based observatories will provide the best simultaneous coverage of these kind of events, providing a complete description of the GRB phenomenon and GRB progenitors up to redshifts $z \gtrsim 9$.

AC acknowledges the anonymous referee for the precious comments in order to improve the quality of this work. The Gemini data, acquired under the program ID GN-20011A-Q-4, are based on observations obtained at the Gemini Observatory, which is operated by the Association of Universities for Research in Astronomy, Inc., under a cooperative agreement with the NSF on behalf of the Gemini partnership: the National Science Foundation (United States), the Science and Technology Facilities Council (United Kingdom), the National Research Council (Canada), CONICYT (Chile), the Australian Research Council (Australia), Ministério da Ciência e Tecnologia (Brazil) and Ministerio de Ciencia, Tecnología e Innovación Productiva (Argentina). A.V.F., S.B.C., and W.L. acknowledge generous financial assistance from Gary & Cynthia Bengier, the Richard & Rhoda Goldman Fund, NASA/*Swift* grants NNX10AI21G and GO-7100028, the TABASGO Foundation, and NSF grant AST-0908886. KAIT and its ongoing operation were made possible by donations from Sun Microsystems, Inc., the Hewlett-Packard Company, AutoScope Corporation, Lick Observatory, the NSF, the University of California, the Sylvia & Jim Katzman Foundation, and the TABASGO Foundation. AC thanks C. Guidorzi and D. A. Kann for the useful discussion and comments.

REFERENCES

- Abazajian, K. N. et al. 2009, ApJS, 182, 543
- Amati, L., Guidorzi, C., Frontera, F., Della Valle, M., Finelli, F., Landi, R., & Montanari, E. 2008, MNRAS, 391, 577

- Barthelmy, S. D. et al. 2005, *Space Science Reviews*, 120, 143
- 2011, GRB Coordinates Network, Circular Service, 11714
- Beardmore, A. P., Baumgartner, W. H., Burrows, D. N., Chester, M. M., & Gelbord, J. M. 2011a, GRB Coordinates Network, Circular Service, 11629
- Beardmore, A. P., Evans, P. A., Goad, M. R., & Osborne, J. P. 2011b, GRB Coordinates Network, Circular Service, 11639
- Bertin, E. & Arnouts, S. 1996, *A&AS*, 117, 393
- Bertin, E., Mellier, Y., Radovich, M., Missonnier, G., Didelon, P., & Morin, B. 2002, in *Astronomical Society of the Pacific Conference Series*, Vol. 281, *Astronomical Data Analysis Software and Systems XI*, ed. D. A. Bohlender, D. Durand, & T. H. Handley, 228
- Beuermann, K. et al. 1999, *A&A*, 352, L26
- Bloom, J. S., Starr, D. L., Blake, C. H., Skrutskie, M. F., & Falco, E. E. 2006, in *Astronomical Society of the Pacific Conference Series*, Vol. 351, *Astronomical Data Analysis Software and Systems XV*, ed. C. Gabriel, C. Arviset, D. Ponz, & S. Enrique, 751
- Breeveld, A. A., Landsman, W., Holland, S. T., Roming, P., Kuin, N. P. M., & Page, M. J. 2011, *ArXiv:1102.4717*
- Burrows, D. N. et al. 2005, *Space Science Reviews*, 120, 165
- Butler, N. R. & Kocevski, D. 2007, *ApJ*, 663, 407
- Butler, N. R., Kocevski, D., Bloom, J. S., & Curtis, J. L. 2007, *ApJ*, 671, 656
- Campana, S., Thöne, C. C., de Ugarte Postigo, A., Tagliaferri, G., Moretti, A., & Covino, S. 2010, *MNRAS*, 402, 2429
- Cenko, S. B. et al. 2006, *PASP*, 118, 1396
- Cenko, S. B., Hora, J. L., & Bloom, J. S. 2011, GRB Coordinates Network, Circular Service, 11638
- Chincarini, G. et al. 2010, *MNRAS*, 406, 2113
- Covino, S., Ghisellini, G., Lazzati, D., & Malesani, D. 2004, in *Astronomical Society of the Pacific Conference Series*, Vol. 312, *Astronomical Society of the Pacific Conference Series*, ed. M. Feroci, F. Frontera, N. Masetti, & L. Piro, 169–+
- Cucchiara, A. et al. 2011, *ApJ*, 736, 7
- da Silva, R., Fumagalli, M., Worsack, G., & Prochaska, X. 2011, GRB Coordinates Network, Circular Service, 11635
- D’Elia, V. et al. 2011, GRB Coordinates Network, Circular Service, 11705
- Evans, P. A. et al. 2009, *MNRAS*, 397, 1177
- 2007, *A&A*, 469, 379
- Fabricant, D., Cheimets, P., Caldwell, N., & Geary, J. 1998, *PASP*, 110, 79
- Falcone, A. D. et al. 2007, *ApJ*, 671, 1921
- Fan, Y.-Z., Dai, Z.-G., Huang, Y.-F., & Lu, T. 2002, *Chinese Journal of Astronomy & Astrophysics*, 2, 449
- Farah, A. et al. 2010, in *Society of Photo-Optical Instrumentation Engineers (SPIE) Conference Series*, ed. Ian S. McLean and Suzanne K. Ramsay and Hideki Takami, Vol. 7735
- Filippenko, A. V., Li, W. D., Treffers, R. R., & Modjaz, M. 2001, in *Astronomical Society of the Pacific Conference Series*, Vol. 246, *IAU Colloq. 183: Small Telescope Astronomy on Global Scales*, ed. B. Paczynski, W.-P. Chen, & C. Lemme, 121–+
- Foley, S. 2011, GRB Coordinates Network, Circular Service, 11727
- Gao, W. 2009, *ApJ*, 697, 1044
- Gao, W.-H. 2011, *ArXiv:1104.3382*
- Gehrels, N. et al. 2004, *ApJ*, 611, 1005
- Golenetskii, S. et al. 2011a, GRB Coordinates Network, Circular Service, 11723
- Golenetskii, S., Aptekar, R., Mazets, E., & Pal’Shin, V. 2011b, GRB Coordinates Network, Circular Service, 11659

- Gomboc, A. et al. 2008, *ApJ*, 687, 443
- Gorosabel, J., Duffard, R., Kubanek, P., & Guirjarro, A. 2011, GRB Coordinates Network, Circular Service, 11696
- Granot, J. & Königl, A. 2003, *ApJ*, 594, L83
- Gruber, D. et al. 2011, *A&A*, 528, A15
- Gruzinov, A. & Waxman, E. 1999, *ApJ*, 511, 852
- Guidorzi, C. et al. 2011, *ArXiv:1105.1591*
— 2006, *PASP*, 118, 288
- Hook, I. M., Jørgensen, I., Allington-Smith, J. R., Davies, R. L., Metcalfe, N., Murowinski, R. G., & Crampton, D. 2004, *PASP*, 116, 425
- Ioka, K., Kobayashi, S., & Zhang, B. 2005, *ApJ*, 631, 429
- Kalberla, P. M. W., Burton, W. B., Hartmann, D., Arnal, E. M., Bajaja, E., Morras, R., & Pöppel, W. G. L. 2005, *A&A*, 440, 775
- Klotz, A. et al. 2008, *A&A*, 483, 847
- Kobayashi, S. 2000, *ApJ*, 545, 807
- Kobayashi, S. & Zhang, B. 2003, *ApJ*, 597, 455
- Kobayashi, S., Zhang, B., Mészáros, P., & Burrows, D. 2007, *ApJ*, 655, 391
- Kumar, P. & Panaitescu, A. 2000, *ApJ*, 541, L51
— 2003, *MNRAS*, 346, 905
- Lazzati, D. & Begelman, M. C. 2006, *ApJ*, 641, 972
- Lazzati, D., Rossi, E., Covino, S., Ghisellini, G., & Malesani, D. 2002, *A&A*, 396, L5
- Liang, E. W. et al. 2006, *ApJ*, 646, 351
- Margutti, R., Bernardini, G., Barniol Duran, R., Guidorzi, C., Shen, R. F., & Chincarini, G. 2011, *MNRAS*, 410, 1064
- Markwardt, C. B. et al. 2011, GRB Coordinates Network, Circular Service, 11646
- Marshall, F. E. et al. 2011, *ApJ*, 727, 132
- Mészáros, A., Řípa, J., & Ryde, F. 2011, *A&A*, 529, A55
- Mészáros, P. 2006, *Reports on Progress in Physics*, 69, 2259
- Miller, J. S. & Stone, R. 1993, Lick Observatory Technical Report (University of California, Santa Cruz), 48
- Molinari, E. et al. 2007, *A&A*, 469, L13
- Morgan, A. N. & Bloom, J. S. 2011, GRB Coordinates Network, Circular Service, 11666
- Morgan, A. N., Klein, C. R., & Bloom, J. S. 2011, GRB Coordinates Network, Circular Service, 11636
- Mundell, C. G., Guidorzi, C., & Steele, I. A. 2010, *Advances in Astronomy*, 2010
- Mundell, C. G. et al. 2007a, *ApJ*, 660, 489
— 2007b, *Science*, 315, 1822
- Oates, S. R. et al. 2011, *MNRAS*, 412, 561
— 2009, *MNRAS*, 395, 490
- Oke, J. B. & Gunn, J. E. 1983, *ApJ*, 266, 713
- Osborne, J. P., Beardmore, A. P., Evans, P. A., & Goad, M. R. 2011, GRB Coordinates Network, Circular Service, 11712
- Pal’Shin, V. 2011, GRB Coordinates Network, Circular Service, 11697
- Panaitescu, A. & Kumar, P. 2002, *ApJ*, 571, 779
- Panaitescu, A. & Vestrand, W. T. 2011, *MNRAS*, 671
- Perley, D. A. et al. 2008, *ApJ*, 672, 449
— 2010, *MNRAS*, 406, 2473
- Petitpas, G., Zauderer, A., Berger, E., Patel, N., Brassfield, E., Miller, J., & Dosaj, A. 2011, GRB Coordinates Network, Circular Service, 11650
- Poole, T. S. et al. 2008, *MNRAS*, 383, 627
- Quimby, R. M. et al. 2006, *ApJ*, 640, 402
- Racusin, J. L. et al. 2008, *Nature*, 455, 183
— 2009, *ApJ*, 698, 43

- Rees, M. J. & Meszaros, P. 1992, *MNRAS*, 258, 41P
- Roming, P. W. A. et al. 2005, *Space Science Reviews*, 120, 95
- Rossi, A. et al. 2011, *A&A*, 529, A142+
- Rossi, E. M., Lazzati, D., Salmonson, J. D., & Ghisellini, G. 2004, *MNRAS*, 354, 86
- Rykoff, E. S. et al. 2004, *ApJ*, 601, 1013
- Sakamoto, T., Barthelmy, S. D., Baumgartner, W. H., & Beardmore, A. P. 2011, GRB Coordinates Network, Circular Service, 11692
- Salvaterra, R. et al. 2009, *Nature*, 461, 1258
- Sari, R. & Piran, T. 1997, *ApJ*, 485, 270
- 1999, *ApJ*, 520, 641
- Sari, R., Piran, T., & Narayan, R. 1998, *ApJ*, 497, L17
- Shao, L. & Dai, Z. G. 2005, *ApJ*, 633, 1027
- Shen, R.-F. & Zhang, B. 2009, *MNRAS*, 398, 1936
- Skrutskie, M. F. et al. 2006, *AJ*, 131, 1163
- Steele, I. A., Bates, S. D., Guidorzi, C., Mottram, C. J., Mundell, C. G., & Smith, R. J. 2010, in *Society of Photo-Optical Instrumentation Engineers (SPIE) Conference Series*, Vol. 7735
- Stratta, G. & D’Elia, V. 2011, GRB Coordinates Network, Circular Service, 11721
- Tanvir, N. R. et al. 2009, *Nature*, 461, 1254
- Totani, T., Kawai, N., Kosugi, G., Aoki, K., Yamada, T., Iye, M., Ohta, K., & Hattori, T. 2006, *PASJ*, 58, 485
- van der Horst, A. J., Kouveliotou, C., Kamble, A. P., & Wijers, R. A. M. J. 2011, GRB Coordinates Network, Circular Service, 11663
- Vestrand, W. T. et al. 2006, *Nature*, 442, 172
- Watson, D., Hjorth, J., Fynbo, J. P. U., Jakobsson, P., Foley, S., Sollerman, J., & Wijers, R. A. M. J. 2007, *ApJ*, 660, L101
- Zauderer, A., Berger, E., & Frail, D. 2011a, GRB Coordinates Network, Circular Service, 11661
- Zauderer, A., Frail, D., & Berger, E. 2011b, GRB Coordinates Network, Circular Service, 11740
- Zhang, B. 2011, *Comptes Rendus Physique*, 12, 206
- Zhang, B., Fan, Y. Z., Dyks, J., Kobayashi, S., Mészáros, P., Burrows, D. N., Nousek, J. A., & Gehrels, N. 2006, *ApJ*, 642, 354
- Zhang, B., Kobayashi, S., & Mészáros, P. 2003, *ApJ*, 595, 950

TABLE 1
BEST FIT TEMPORAL PARAMETERS

Event	α_1	β_1	$t_{b,1}$	α_2	β_2	$t_{b,2}$
GRB 110205A	-6.13 ± 0.75	1.71 ± 0.28	837^{+51}_{-40}	-0.48 ± 0.22	1.74 ± 0.28	68980
GRB 110213A	-2.08 ± 0.23	1.10 ± 0.24	263^{+13}_{-19}	-2.02 ± 0.34	1.80 ± 0.15	4827

NOTE.—Best-fit parameters for GRB110205A and GRB110213A using the sum of two Beuermann function (Beuermann et al. 1999). The multiband fit has been obtain simultaneously in all the observed optical and NIR bands.

TABLE 2
ABSORPTION LINES IN THE AFTERGLOW SPECTRUM OF GRB 110205A

λ (\AA)	z	Transition	W^a (\AA)	$\sigma(W)^b$ (\AA)
4030.00	2.21420	SiII 1253	< 1.10	
4184.83	2.21374	OI 1302	0.69	0.23
4289.89	2.21453	CII 1334	1.31	0.25
4479.97	2.21432	SiIV 1393	< 1.09	
4907.11	2.21418	SiII 1526	0.99	0.17
4927.55	2.21432	SiII* 1533	0.54	0.16
4977.05	2.21474	CIV 1548	0.73	0.20
5170.77	2.21408	FeII 1608	0.86	0.16
5371.76	2.21510	AlII 1670	1.04	0.15
5909.44			2.40	0.59
5962.61	2.21484	AlIII 1854	1.18	0.19
6514.62	2.21529	ZnII 2026	< 0.51	

^aEquivalent widths are rest-frame values and assume the redshift given in Column 2.

^bUncertainties are 2σ statistical values.

TABLE 3
 ABSORPTION LINES IN THE AFTERGLOW SPECTRUM OF GRB 110213A

λ (Å)	z	Transition	W^a (Å)	$\sigma(W)^b$ (Å)
4112.10	1.46233	AlIII 1670	1.96	0.33
4238.78			2.39	0.68
4566.75	1.46311	AlIII 1854	1.73	0.21
4984.60	1.45934	ZnII 2026	< 0.60	
5310.17			2.77	0.29
5354.79	1.46197	NiII* 2175	1.16	0.11
5404.37			3.12	0.27
5433.04			2.27	0.27
5471.65	1.46138	NiII* 2223	1.82	0.11
5767.82	1.46067	FeII 2344	3.51	0.09
5859.36			13.31	0.22
5893.38	1.45967	FeII* 2396a	4.54	0.09
5918.62	1.46096	FeII* 2405	6.89	0.09
6237.86			80.12	0.22
5998.19			6.16	0.22
6062.10	1.46126	FeI 2463	1.01	0.09
6089.69			2.14	0.21
6135.74			1.29	0.21
6196.43			4.30	0.21
6286.07			5.45	0.21
6363.63	1.46080	FeII 2586	2.73	0.08
6397.78	1.46068	FeII 2600	3.31	0.08
6475.33	1.46116	FeII* 2631	1.76	0.08
6530.68			3.51	0.20
6562.87			4.03	0.20
6786.08	1.46229	FeII* 2756	1.20	0.07
7018.68	1.46010	MgI 2853	1.81	0.19

^aEquivalent widths are rest-frame values and assume the redshift given in Column 2.

^bUncertainties are 2σ statistical values.

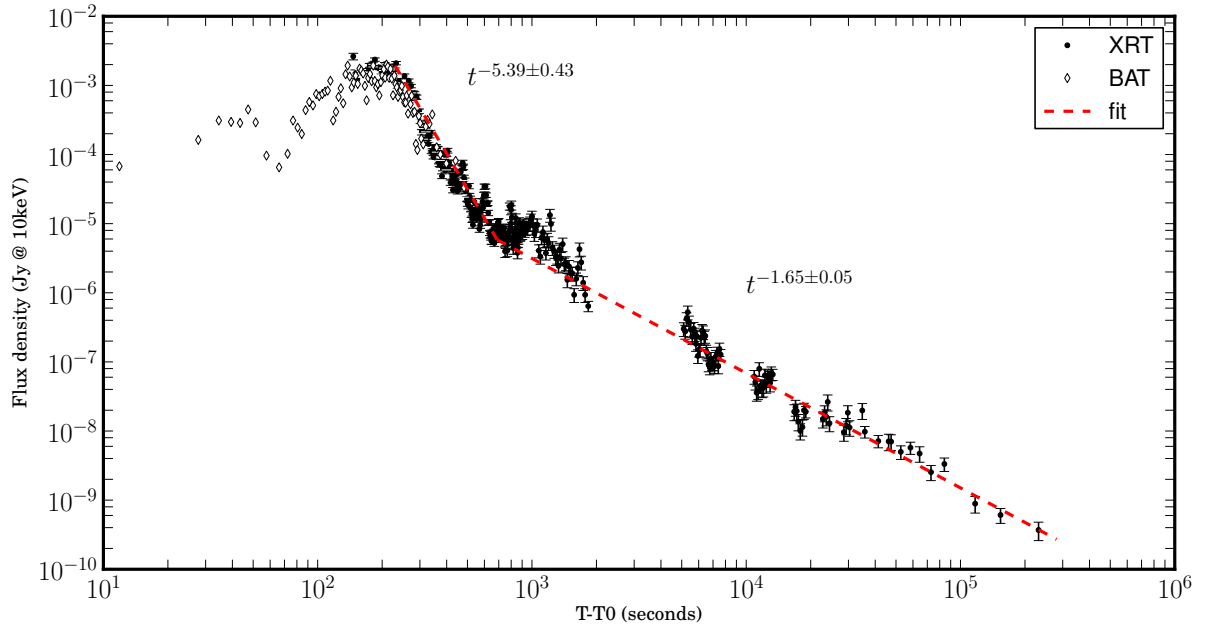


Fig. 1.— GRB110205A BAT (open diamonds) and XRT (filled circles) lightcurve. The BAT emission is rescaled to the XRT energy bands using a spectral index $\Gamma_{\text{ave}} = 1.59$ (see §4.1.1). Dashed lines indicate the different power-law segments obtained by fitting the XRT data with single power-laws.

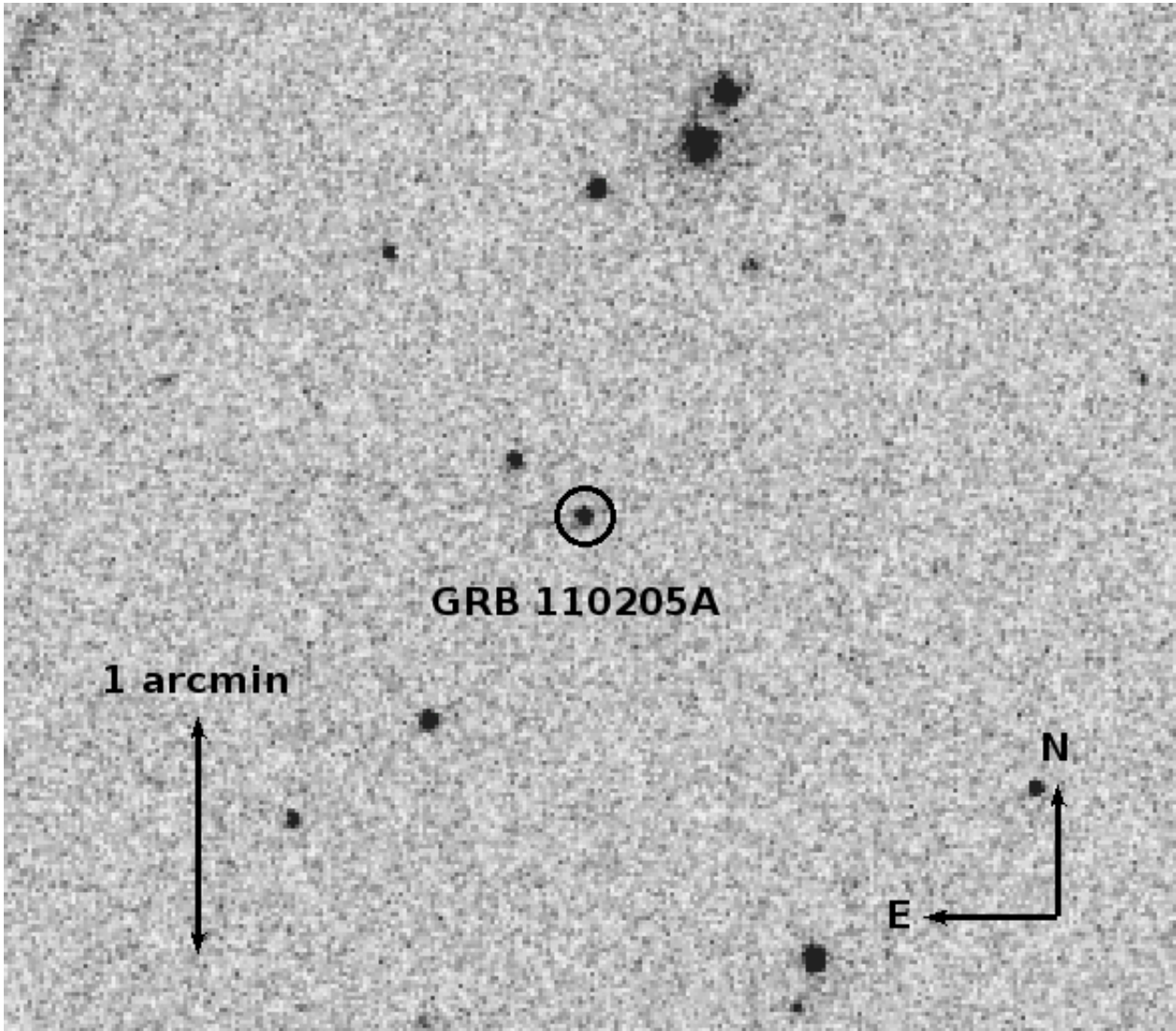


Fig. 2.— UVOT v band image of GRB 110205A obtained ~ 1400 s after the trigger.

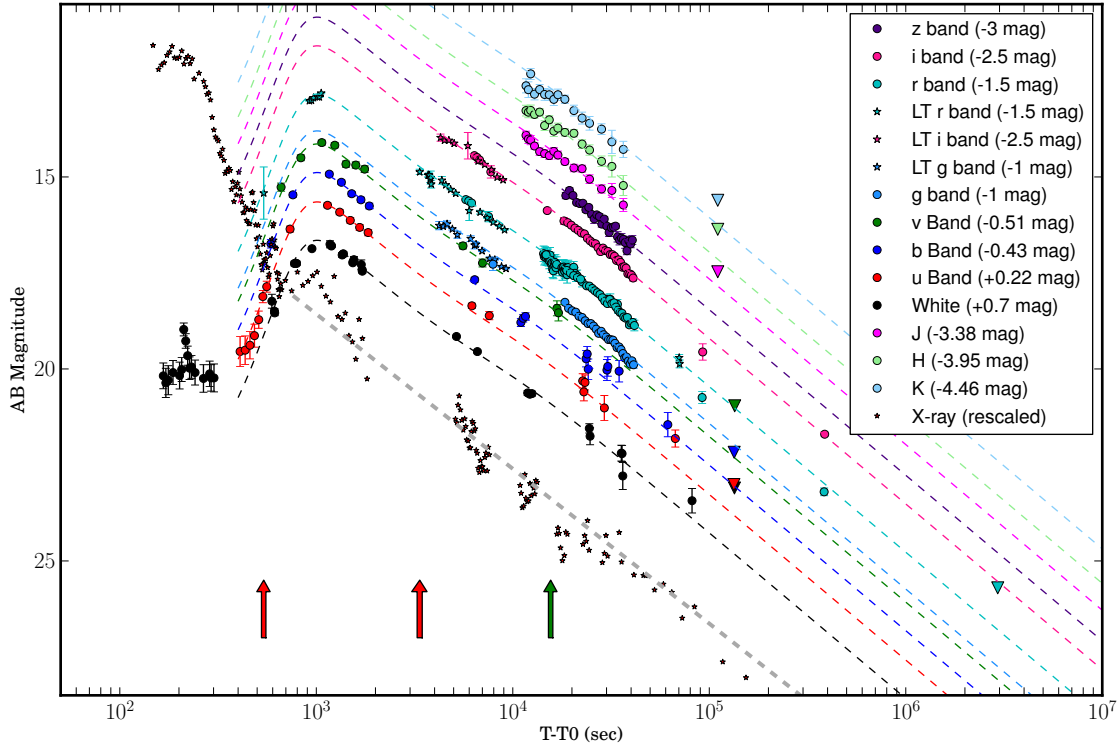


Fig. 3.— GRB110205A lightcurve. We present all the available public data in conjunction with the datasets present in this work. The dashed lines represent a resulting multiband fit (see §2 for more details). The XRT light curve is arbitrarily rescaled for comparison and fitted with a simple power-law function. The achromatic step rise in the optical bands is interpreted as the signature of the reverse shock. After the peak at $T \approx 985$ s the forward shock is the main source of radiation, confirmed by the net polarization measurement obtained at the time of the RINGO2 and the CAFOS instruments observations, indicated with red and green arrows, respectively.

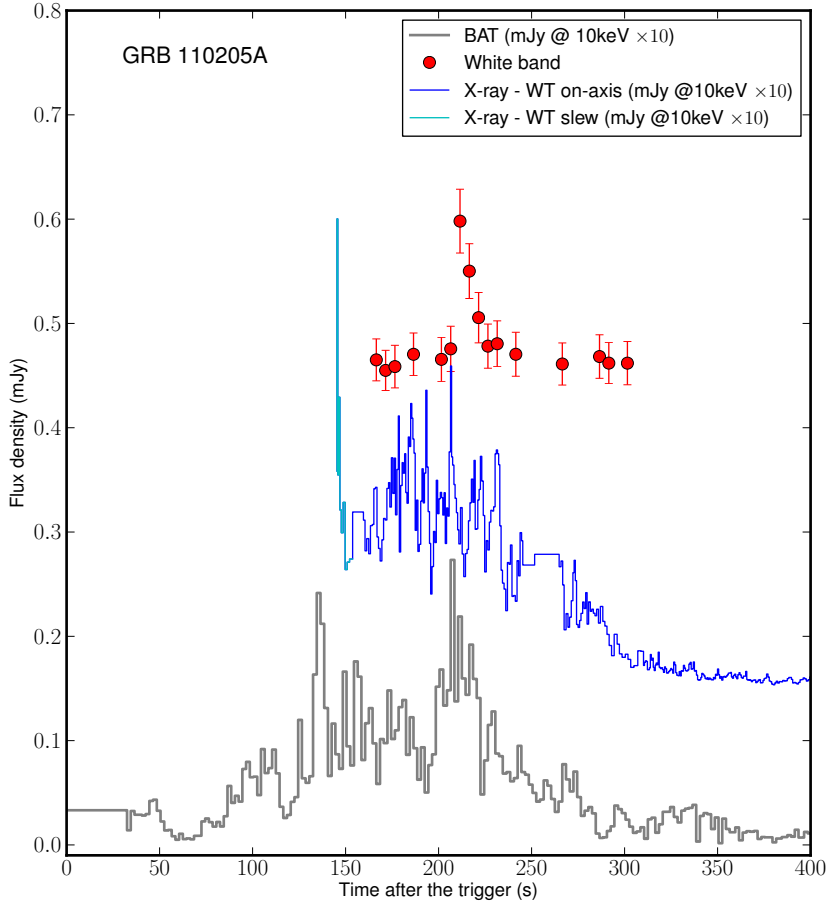


Fig. 4.— Early time light curve comparison. The BAT flux density (grey histogram, 1-sec bin) has been extrapolated in the XRT bandpass (0.3–10 keV). Red points are UVOT *white* band detections (5 s bin), while the cyan and blue points are XRT window-timing mode detections (0.5 s bin) during and after the slewing procedure respectively. There is a hint of correlation between the optical and the high-energy bands, probably indicative of a similar emission mechanism during the prompt phase. The three curves have been shifted along the ordinate to facilitate this comparison.

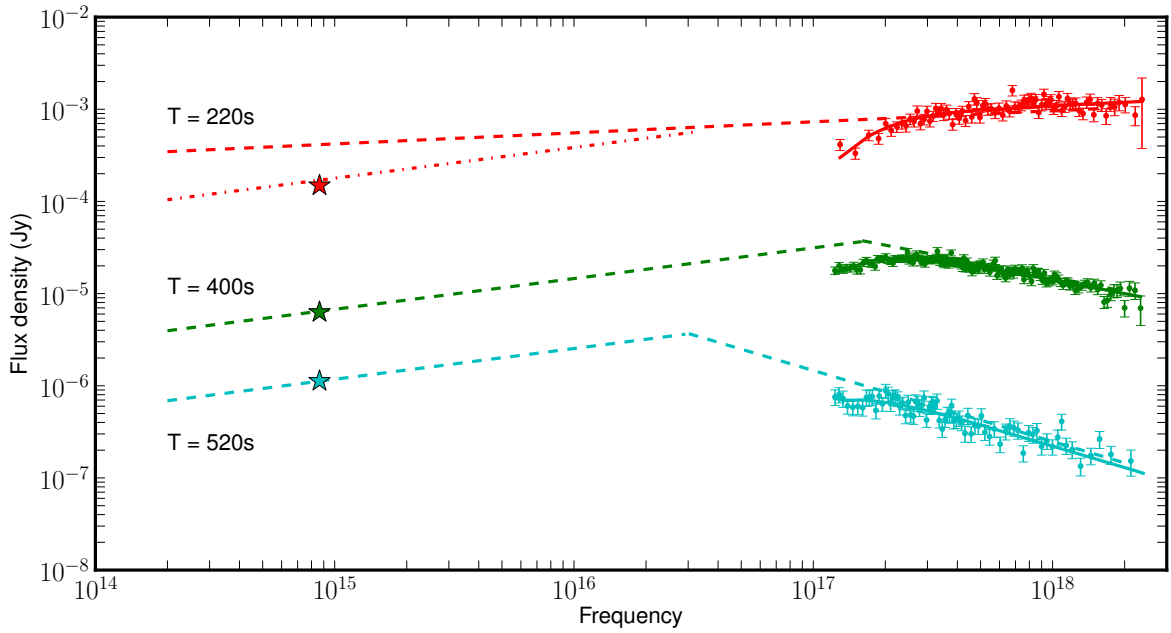


Fig. 5.— Spectral energy distribution constructed using the XRT and the UVOT *white*-band data at the time of the optical peak ($T \approx 220$ s), at $T \approx 400$ s, and at $T \approx 520$ s, when the high-latitude effect likely dominates the observed emission. Fitting the SED at the peak with a broken power law, as shown by the dashed-dotted line (imposing a spectral index $\beta = 1/3$ at $\nu_{\text{opt}} < \nu < \nu_X$), implies a spectral break which is inconsistent with the spectral evolution at later times. The most likely scenario is that the *white*-band detection is affected by attenuation due to the DLA and the broad-band transmission curve of the UVOT filter.

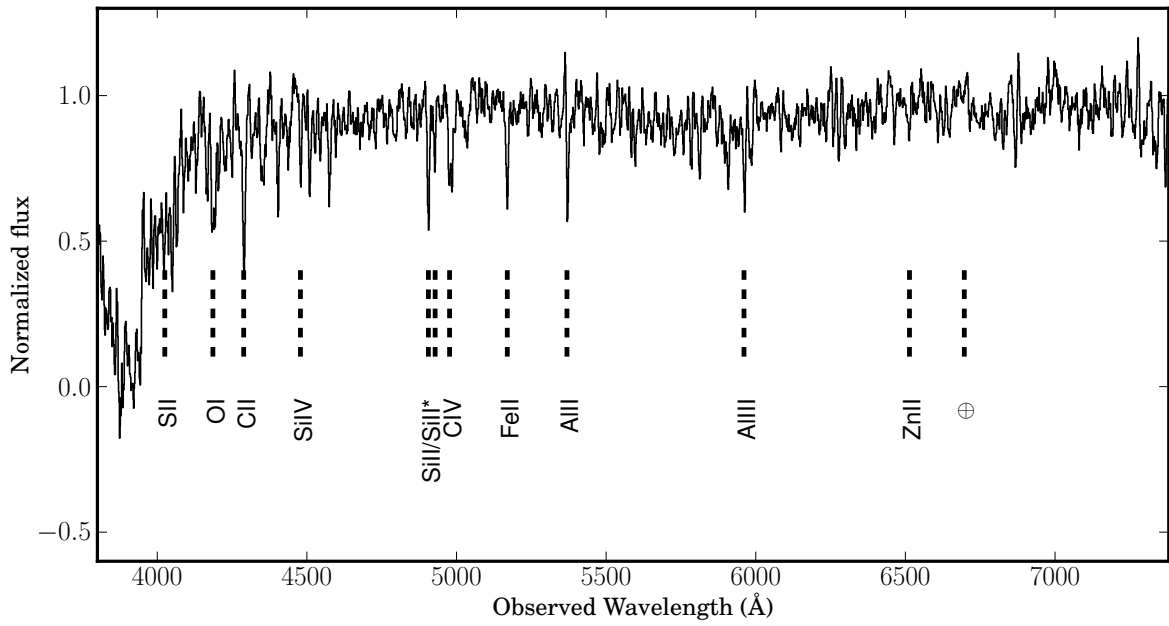


Fig. 6.— Normalized spectrum of the afterglow of GRB 110205A obtained with the FAST spectrograph ~ 3.5 h after the burst (see Sec. 2.4 for details). The main absorption features are labeled as well the main atmospheric absorption bands.

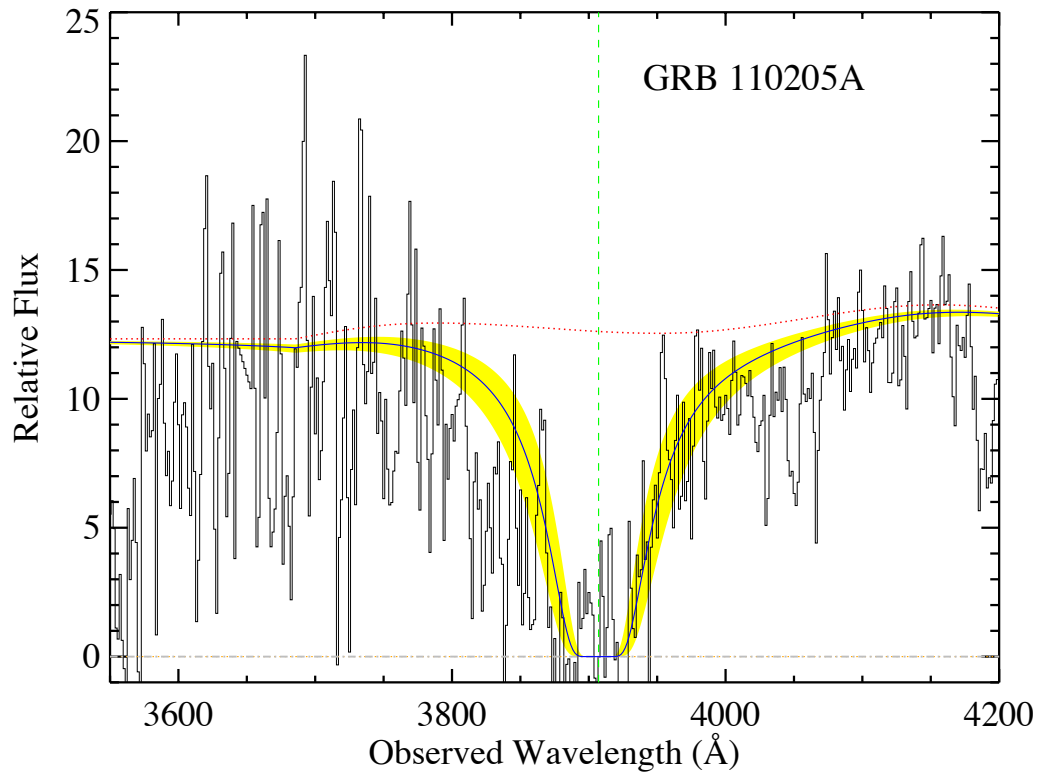


Fig. 7.— Portion of the spectrum obtained with the Kast spectrograph at Lick Observatory. A DLA absorption system is clearly detected, placing GRB 110205A at $z = 2.22$. The blue line represents the DLA fit, while the shaded area is the 1σ confidence interval. The dotted red line is the continuum fit and the green dashed line identifies the location of the 1216 \AA Ly- α feature. A Voigt profile fit gives a neutral hydrogen column density of $\log(N_{\text{H}}/\text{cm}^{-2}) = 21.45 \pm 0.23$.

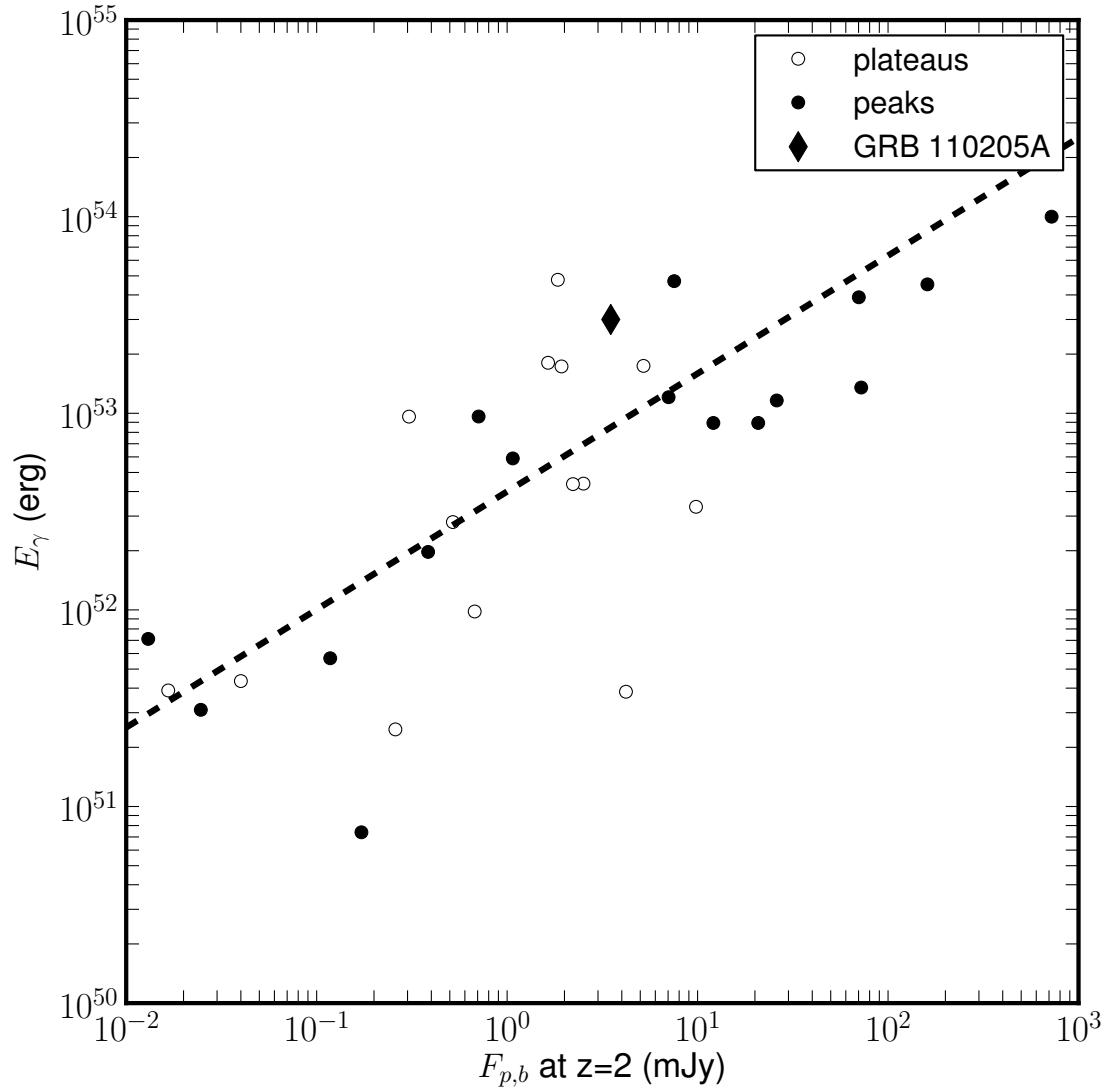


Fig. 8.— Figure adopted from Panaitescu & Vestrand (2011). The abscissa represents the optical flux at the observed peak time, F_p (or at the end of an extended plateau phase, T_b). GRB 110205A is plotted as a filled diamond and presents a peak luminosity compared to other “peaky” afterglow cases (filled circles) or GRBs that present plateau phases (open circles). The dashed line represents the correlation between these fluxes and the isotropic equivalent energy released (E_{γ}). As mentioned by these authors the rising in the light curve may be due to a deceleration of the fireball which implies a large release of energy in a short amount of time.

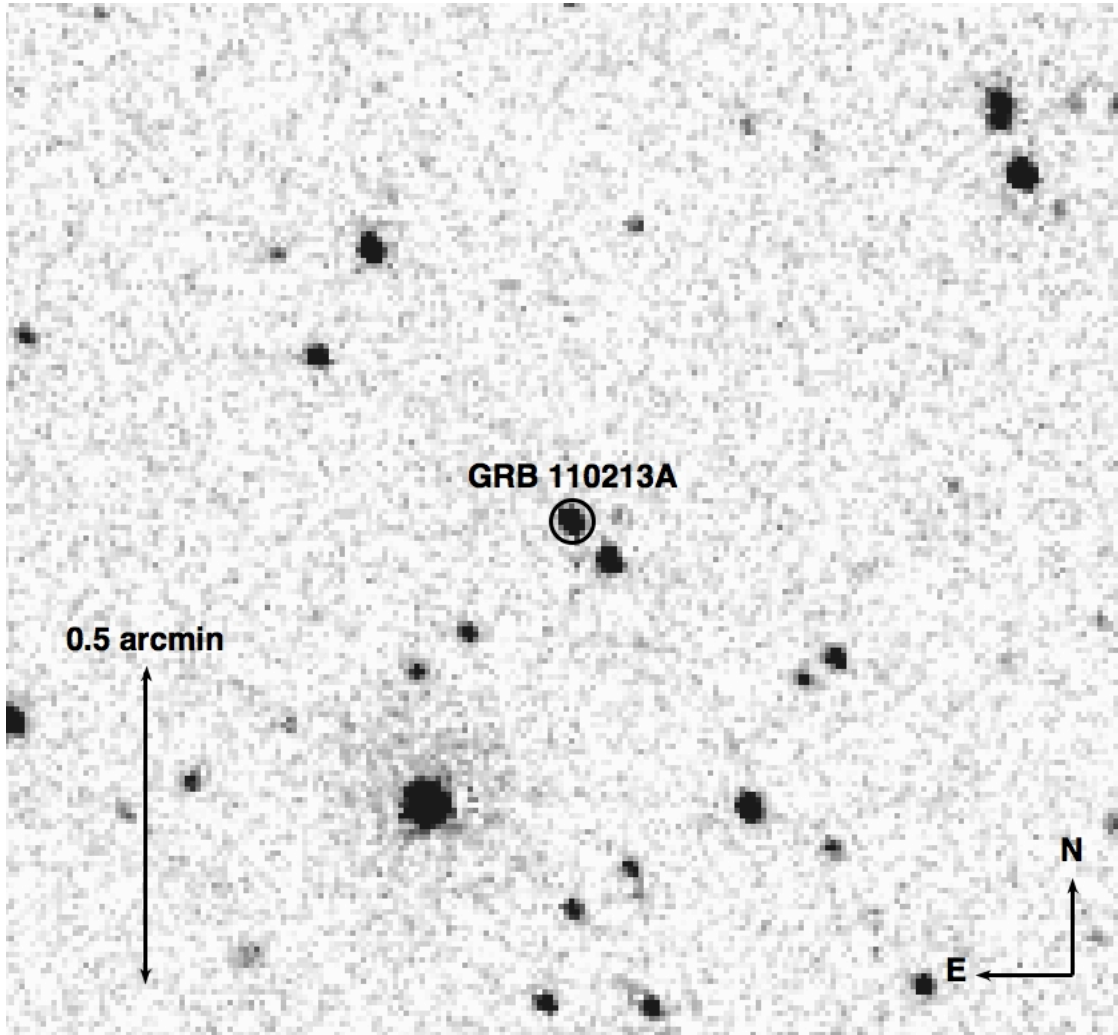


Fig. 9.— UVOT *v* band image of GRB 110213A obtained ~ 650 s after the trigger.

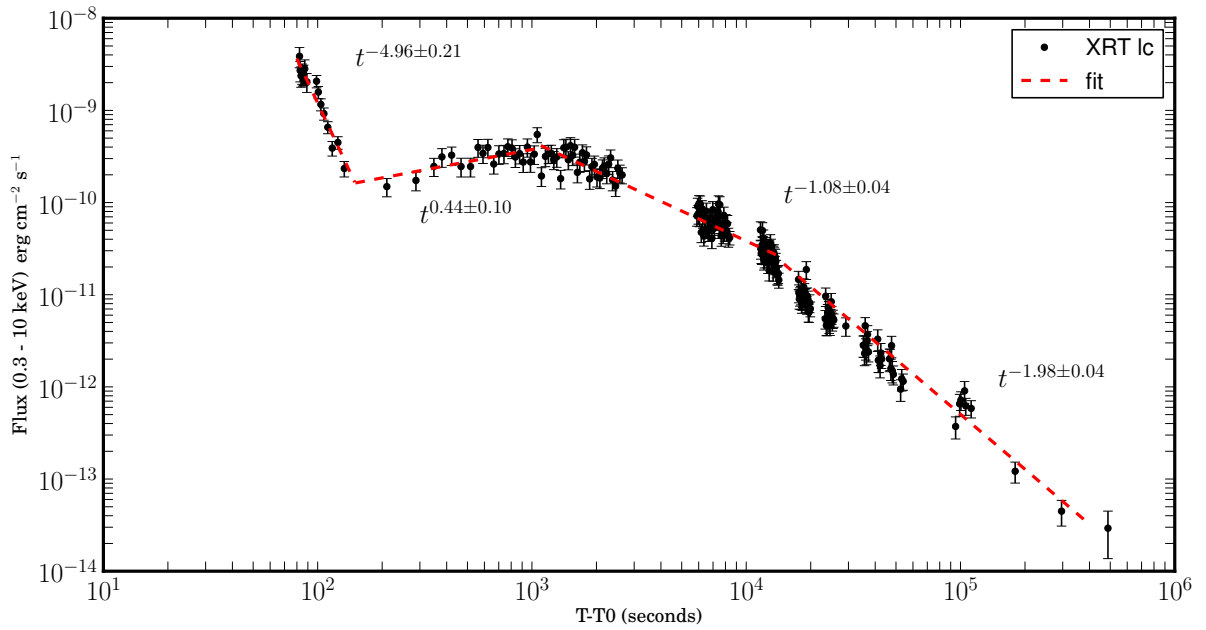


Fig. 10.— GRB110213A XRT lightcurve. Dashed lines indicate the different power-law segments obtained fitting the XRT data with single power-laws.

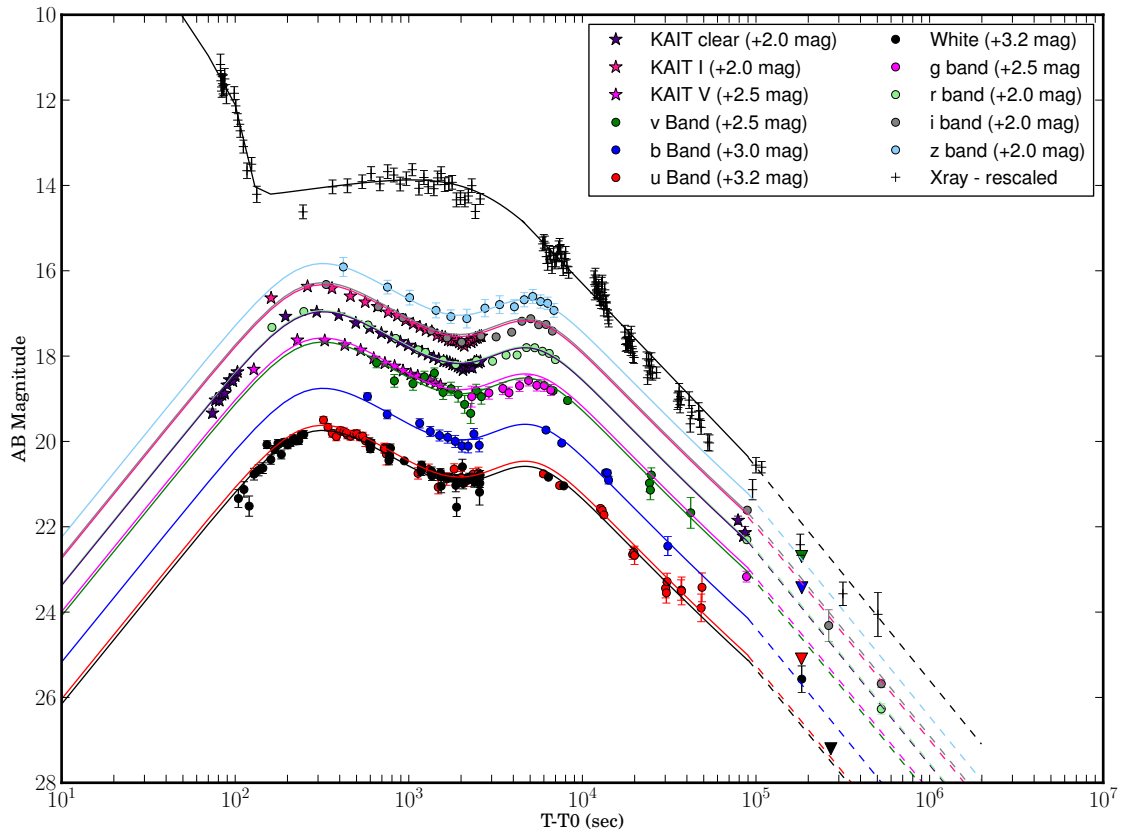


Fig. 11.— GRB110213A lightcurve. We represent all the datasets present in this work. All of the magnitudes are transformed into AB systems (Oke & Gunn 1983). We interpret the two peaks as the onset of the afterglow and the continuous energy injection from a long living central engine.

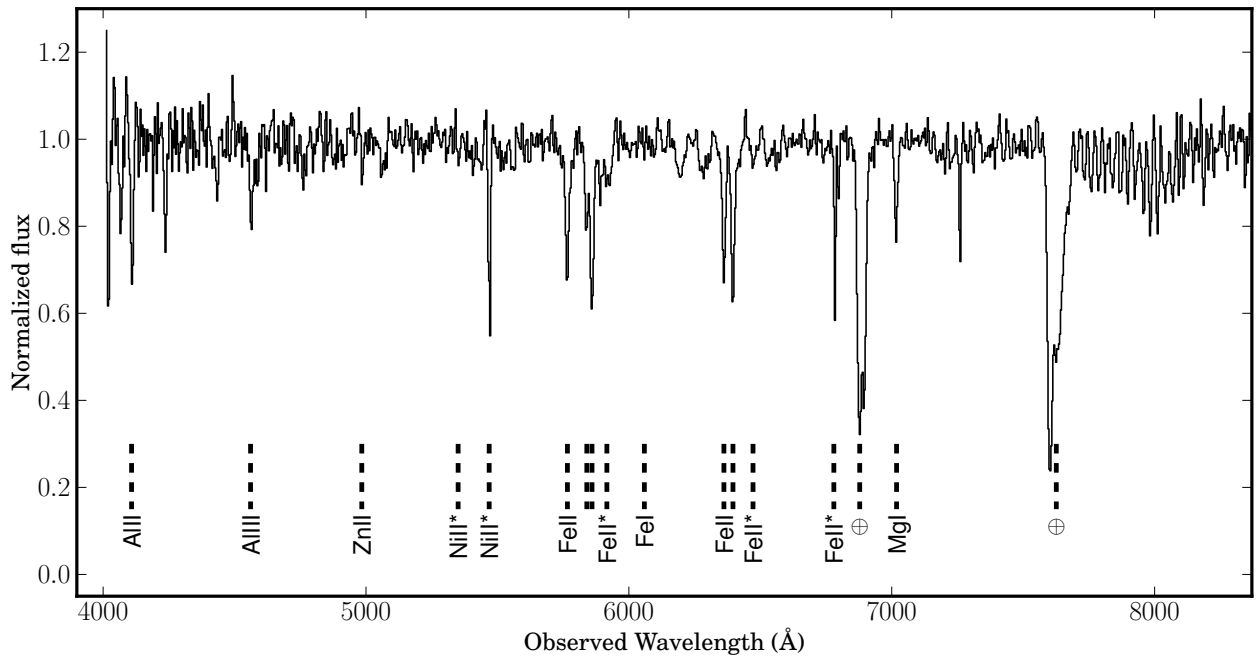


Fig. 12.— Normalized spectrum of the afterglow of GRB 110213A obtained with the Bok spectrograph. The main absorption features are labeled, as are the telluric lines.

TABLE 4
PHOTOMETRIC OBSERVATIONS FOR GRB 110205A

$T - T_0$ (s)	Filter	Magnitude ^a	1σ Error
<i>Swift</i> -UVOT			
166	<i>white</i>	18.68	0.34
171	<i>white</i>	18.86	0.38
176	<i>white</i>	18.79	0.38
186	<i>white</i>	18.59	0.31
201	<i>white</i>	18.67	0.35
206	<i>white</i>	18.52	0.31
211	<i>white</i>	17.47	0.17
216	<i>white</i>	17.77	0.19
221	<i>white</i>	18.15	0.25
226	<i>white</i>	18.48	0.29
231	<i>white</i>	18.45	0.30
241	<i>white</i>	18.59	0.32
266	<i>white</i>	18.75	0.36
286	<i>white</i>	18.63	0.33
291	<i>white</i>	18.73	0.34
301	<i>white</i>	18.73	0.36
601	<i>white</i>	16.74	0.18
606	<i>white</i>	17.24	0.15
611	<i>white</i>	17.03	0.13
616	<i>white</i>	16.95	0.13
621	<i>white</i>	16.89	0.17
776	<i>white</i>	15.73	0.09
781	<i>white</i>	15.78	0.08
786	<i>white</i>	15.70	0.08
791	<i>white</i>	15.80	0.08
1181	<i>white</i>	15.25	0.09
1186	<i>white</i>	15.20	0.07
1191	<i>white</i>	15.40	0.07
1196	<i>white</i>	15.27	0.07
1201	<i>white</i>	15.37	0.12
1356	<i>white</i>	15.45	0.09
1361	<i>white</i>	15.58	0.08
1366	<i>white</i>	15.55	0.08
1371	<i>white</i>	15.55	0.08
1376	<i>white</i>	15.25	0.12
1531	<i>white</i>	15.73	0.08
1536	<i>white</i>	15.76	0.08
1541	<i>white</i>	15.76	0.08
1546	<i>white</i>	15.65	0.08
1701	<i>white</i>	15.78	0.12
1706	<i>white</i>	15.65	0.08
1711	<i>white</i>	16.20	0.09
1716	<i>white</i>	15.96	0.09
1721	<i>white</i>	16.13	0.13
5166	<i>white</i>	17.67	0.04
6602	<i>white</i>	18.07	0.04
11906	<i>white</i>	19.15	0.06
12210	<i>white</i>	19.16	0.06
12513	<i>white</i>	19.15	0.06
24517	<i>white</i>	20.04	0.12
24734	<i>white</i>	20.25	0.22

TABLE 4—*Continued*

$T - T_0$ (s)	Filter	Magnitude ^a	1σ Error
35676	<i>white</i>	20.69	0.21
35979	<i>white</i>	20.70	0.21
36284	<i>white</i>	21.28	0.35
81699	<i>white</i>	21.93	0.32
134282	<i>white</i>	> 23.79	

^aUVOT magnitude are in the natural UVOT photometric system (Vega). See Breeveld et al. (2011) for the most updated zeropoint and conversion factors.

TABLE 5
PHOTOMETRIC OBSERVATIONS FOR GRB 110205A

$T - T_0$ (s)	Filter	Magnitude ^a	1σ Error
<i>Swift-UVOT</i>			
409	<i>u</i>	18.75	0.39
434	<i>u</i>	18.71	0.37
459	<i>u</i>	18.58	0.35
484	<i>u</i>	18.33	0.30
509	<i>u</i>	17.92	0.22
534	<i>u</i>	17.32	0.16
559	<i>u</i>	17.06	0.14
734	<i>u</i>	15.58	0.08
1134	<i>u</i>	14.97	0.07
1159	<i>u</i>	14.88	0.14
1309	<i>u</i>	15.15	0.07
1334	<i>u</i>	14.98	0.15
1484	<i>u</i>	15.30	0.07
1659	<i>u</i>	15.53	0.08
1834	<i>u</i>	15.67	0.09
47582	<i>u</i>	20.65	0.48
67156	<i>u</i>	21.01	0.22
133453	<i>u</i>	> 23.31	

^aUVOT magnitude are in the natural UVOT photometric system (Vega). See Breeveld et al. (2011) for the most updated zeropoint and conversion factors.

TABLE 6
PHOTOMETRIC OBSERVATIONS FOR GRB 110205A

$T - T_0$ (s)	Filter	Magnitude ^a	1σ Error
<i>Swift</i> -UVOT			
587	<i>b</i>	17.08	0.12
747	<i>b</i>	15.80	0.10
767	<i>b</i>	15.77	0.08
1147	<i>b</i>	15.32	0.13
1167	<i>b</i>	15.22	0.06
1327	<i>b</i>	15.41	0.10
1347	<i>b</i>	15.47	0.07
1507	<i>b</i>	15.77	0.08
1527	<i>b</i>	15.72	0.11
1687	<i>b</i>	15.92	0.07
1847	<i>b</i>	16.01	0.12
1867	<i>b</i>	16.11	0.09
6397	<i>b</i>	17.99	0.06
10993	<i>b</i>	19.10	0.11
11297	<i>b</i>	19.00	0.10
11601	<i>b</i>	18.97	0.10
23604	<i>b</i>	20.10	0.23
23908	<i>b</i>	20.10	0.24
24212	<i>b</i>	20.45	0.31
30449	<i>b</i>	20.38	0.30
34763	<i>b</i>	20.36	0.28
61506	<i>b</i>	21.75	0.31
133867	<i>b</i>	> 22.63	

^aUVOT magnitude are in the natural UVOT photometric system (Vega). See Breeveld et al. (2011) for the most updated zeropoint and conversion factors.

TABLE 7
PHOTOMETRIC OBSERVATIONS FOR GRB 110205A

$T - T_0$ (s)	Filter	Magnitude ^a	1σ Error
<i>Swift</i> -UVOT			
655	<i>v</i>	15.88	0.14
675	<i>v</i>	15.63	0.18
835	<i>v</i>	15.04	0.08
1055	<i>v</i>	14.62	0.09
1075	<i>v</i>	14.65	0.09
1235	<i>v</i>	14.65	0.08
1255	<i>v</i>	14.80	0.12
1415	<i>v</i>	15.19	0.08
1575	<i>v</i>	15.10	0.13
1595	<i>v</i>	15.26	0.10
1755	<i>v</i>	15.24	0.10
1775	<i>v</i>	15.52	0.17
5576	<i>v</i>	17.34	0.08
7013	<i>v</i>	17.79	0.11
16772	<i>v</i>	19.04	0.22
17076	<i>v</i>	19.17	0.25
17379	<i>v</i>	19.10	0.23
134686	<i>v</i>	> 22.82	

^aUVOT magnitude are in the natural UVOT photometric system (Vega). See Breeveld et al. (2011) for the most updated zeropoint and conversion factors.

TABLE 8
PHOTOMETRIC OBSERVATIONS FOR GRB 110205A

$T - T_0$ (s)	Filter	Magnitude	1σ Error
Palomar telescope			
7929	g'	18.272	0.162
18421	g'	19.265	0.036
19229	g'	19.421	0.028
20026	g'	19.485	0.013
20913	g'	19.522	0.019
21730	g'	19.627	0.019
22533	g'	19.659	0.019
23350	g'	19.746	0.019
24158	g'	19.819	0.022
24961	g'	19.819	0.017
25763	g'	19.883	0.039
26561	g'	19.964	0.032
27358	g'	20.072	0.027
28175	g'	20.02	0.026
28984	g'	20.109	0.022
29886	g'	20.168	0.024
30704	g'	20.235	0.024
31531	g'	20.238	0.041
32334	g'	20.25	0.03
33131	g'	20.333	0.026
33934	g'	20.444	0.032
34741	g'	20.427	0.042
35538	g'	20.495	0.048
36331	g'	20.599	0.058
37128	g'	20.714	0.032
37921	g'	20.69	0.042
38714	g'	20.795	0.06
39579	g'	20.873	0.06
40372	g'	20.788	0.061
41164	g'	20.891	0.093
Liverpool Telescope			
4221	g'	17.266	0.109
4423	g'	17.286	0.039
4630	g'	17.226	0.109
4926	g'	17.356	0.109
5223	g'	17.506	0.109
6103	g'	17.606	0.109
6393	g'	17.776	0.109
6500	g'	17.756	0.109
6976	g'	17.926	0.109
7631	g'	18.126	0.109
8105	g'	18.156	0.109
8763	g'	18.336	0.109
9239	g'	18.386	0.109

TABLE 9
PHOTOMETRIC OBSERVATIONS FOR GRB 110205A

$T - T_0$ (s)	Filter	Magnitude	1σ Error
KAIT telescope			
14344	r'	18.499	0.200
14470	r'	18.577	0.217
14594	r'	18.543	0.225
14719	r'	18.540	0.194
14844	r'	18.608	0.200
14968	r'	18.518	0.182
15093	r'	18.588	0.208
15218	r'	18.632	0.190
15343	r'	18.686	0.205
15468	r'	18.535	0.199
15593	r'	18.670	0.208
15717	r'	18.769	0.216
15842	r'	18.735	0.204
15965	r'	18.899	0.221
16090	r'	18.944	0.206
16214	r'	18.720	0.189
16338	r'	18.797	0.219
16462	r'	18.733	0.208
16587	r'	18.863	0.211
16712	r'	18.778	0.198
17781	r'	18.863	0.198
17905	r'	18.980	0.211
18028	r'	18.873	0.193
18153	r'	18.848	0.195
18278	r'	18.921	0.182
18400	r'	18.962	0.189
18523	r'	18.875	0.189
18647	r'	18.889	0.196
18772	r'	18.917	0.194
18897	r'	19.045	0.219
19021	r'	18.929	0.202
19146	r'	18.860	0.191
20127	r'	18.974	0.148
20408	r'	18.852	0.147
20686	r'	19.010	0.145
20970	r'	19.081	0.139
21254	r'	19.072	0.146
22514	r'	19.228	0.136
30129	r'	19.690	0.136
31342	r'	19.687	0.142
34080	r'	19.816	0.126
Palomar Telescope			
5766	r'	17.090	0.018
5969	r'	17.126	0.013
6172	r'	17.180	0.015
7528	r'	17.533	0.134
14775	r'	18.526	0.045
18823	r'	18.935	0.019
19625	r'	19.000	0.018

TABLE 9—*Continued*

$T - T_0$ (s)	Filter	Magnitude	1σ Error
20428	r'	19.069	0.015
21324	r'	19.119	0.017
22127	r'	19.159	0.024
23752	r'	19.335	0.026
24554	r'	19.343	0.028
25357	r'	19.403	0.039
26164	r'	19.464	0.041
26957	r'	19.514	0.036
27764	r'	19.561	0.024
28578	r'	19.646	0.035
29390	r'	19.735	0.019
30303	r'	19.797	0.030
31125	r'	19.692	0.036
31928	r'	19.800	0.022
32730	r'	19.779	0.033
33528	r'	19.889	0.039
34331	r'	19.969	0.081
35143	r'	20.029	0.028
35935	r'	20.050	0.030
36733	r'	20.147	0.042
37525	r'	20.177	0.036
38317	r'	20.161	0.045
39183	r'	20.351	0.055
39976	r'	20.306	0.038
40768	r'	20.288	0.093
41561	r'	20.369	0.138
91963	r'	22.244	0.153
Liverpool Telescope			
540	r'	16.92	0.68
922.2	r'	14.518	0.011
945	r'	14.508	0.011
967.8	r'	14.438	0.013
1015	r'	14.418	0.013
1037	r'	14.418	0.012
1059	r'	14.318	0.015
3360	r'	16.37	0.07
3708	r'	16.458	0.046
3730	r'	16.448	0.048
3752	r'	16.458	0.059
3798	r'	16.558	0.084
3821	r'	16.518	0.171
3843	r'	16.688	0.101
4355	r'	16.588	0.102
4559	r'	16.708	0.012
4827	r'	16.828	0.007
5124	r'	16.928	0.027
6003	r'	17.378	0.258
6818	r'	17.418	0.05
7413	r'	17.568	0.012
7947	r'	17.678	0.009
8544	r'	17.778	0.014

TABLE 9—*Continued*

$T - T_0$ (s)	Filter	Magnitude	1σ Error
9081	r'	17.878	0.009
7.029e+04	r'	21.208	0.086
7.06e+04	r'	21.368	0.103
Gemini-N Telescope			
384191	r'	23.450	0.050
2937600	r'	> 27.21	

TABLE 10
PHOTOMETRIC OBSERVATIONS FOR GRB 110205A

$T - T_0$ (s)	Filter	Magnitude	1σ Error
Palomar telescope			
6375	<i>i'</i>	16.945	0.019
6574	<i>i'</i>	16.992	0.015
6772	<i>i'</i>	17.057	0.018
7731	<i>i'</i>	17.368	0.161
14973	<i>i'</i>	18.376	0.045
18214	<i>i'</i>	18.646	0.09
19031	<i>i'</i>	18.689	0.017
19828	<i>i'</i>	18.756	0.013
20710	<i>i'</i>	18.833	0.018
21527	<i>i'</i>	18.89	0.013
22330	<i>i'</i>	18.957	0.03
23152	<i>i'</i>	18.984	0.024
23955	<i>i'</i>	19.095	0.019
24757	<i>i'</i>	19.164	0.019
25560	<i>i'</i>	19.22	0.028
26362	<i>i'</i>	19.241	0.033
27160	<i>i'</i>	19.341	0.022
27972	<i>i'</i>	19.444	0.06
28776	<i>i'</i>	19.353	0.045
29593	<i>i'</i>	19.417	0.024
30500	<i>i'</i>	19.438	0.038
31333	<i>i'</i>	19.522	0.042
32131	<i>i'</i>	19.524	0.039
32928	<i>i'</i>	19.566	0.036
33731	<i>i'</i>	19.675	0.044
34538	<i>i'</i>	19.658	0.075
35341	<i>i'</i>	19.724	0.033
36133	<i>i'</i>	19.851	0.048
36930	<i>i'</i>	19.838	0.057
37723	<i>i'</i>	19.876	0.048
38515	<i>i'</i>	20.021	0.048
39382	<i>i'</i>	20.027	0.078
40174	<i>i'</i>	20.057	0.038
40966	<i>i'</i>	20.132	0.078
92572	<i>i'</i>	22.058	0.213
386587	<i>i'</i>	23.45	0.05
Liverpool Telescope			
4289	<i>i'</i>	16.477	0.093
4491	<i>i'</i>	16.547	0.016
4729	<i>i'</i>	16.547	0.008
5028	<i>i'</i>	16.627	0.032
5906	<i>i'</i>	16.687	0.345
6660	<i>i'</i>	17.087	0.035
7196	<i>i'</i>	17.177	0.013
7789	<i>i'</i>	17.317	0.044
8326	<i>i'</i>	17.507	0.013
8923	<i>i'</i>	17.577	0.013

TABLE 11
 PHOTOMETRIC OBSERVATIONS FOR GRB 110205A

$T - T_0$ (s)	Filter	Magnitude	1σ Error
Palomar telescope			
18620	z'	18.485	0.081
19427	z'	18.352	0.068
20230	z'	18.482	0.032
21121	z'	18.665	0.038
21929	z'	18.694	0.036
22731	z'	18.686	0.051
23549	z'	18.854	0.068
24357	z'	18.793	0.055
25158	z'	18.974	0.072
25966	z'	19.092	0.123
26758	z'	18.988	0.058
27561	z'	19.03	0.076
28374	z'	19.228	0.08
29187	z'	19.097	0.058
30094	z'	19.281	0.06
30927	z'	19.446	0.105
31730	z'	19.322	0.066
32532	z'	19.304	0.063
33329	z'	19.282	0.061
34132	z'	19.56	0.134
34945	z'	19.646	0.124
35737	z'	19.594	0.124
36534	z'	19.626	0.086
37327	z'	19.708	0.15
38119	z'	19.922	0.102
38985	z'	19.667	0.109
39777	z'	19.745	0.098
40570	z'	19.645	0.117

TABLE 12
PHOTOMETRIC OBSERVATIONS FOR GRB 110205A

$T - T_0$ (s)	Filter	Magnitude ^a	1σ Error
PAIRITEL			
11677	<i>J</i>	16.416	0.106
12004	<i>J</i>	16.514	0.114
12333	<i>J</i>	16.540	0.120
12897	<i>J</i>	16.695	0.085
13695	<i>J</i>	16.841	0.097
14513	<i>J</i>	16.893	0.100
15332	<i>J</i>	16.946	0.104
16170	<i>J</i>	16.834	0.096
16969	<i>J</i>	16.929	0.102
18407	<i>J</i>	17.101	0.081
20464	<i>J</i>	17.267	0.096
22523	<i>J</i>	17.285	0.090
24580	<i>J</i>	17.558	0.114
28290	<i>J</i>	17.813	0.109
31929	<i>J</i>	17.852	0.179
36517	<i>J</i>	18.230	0.167

^aPAIRITEL Magnitude are in Vega system.

TABLE 13
PHOTOMETRIC OBSERVATIONS FOR GRB 110205A

$T - T_0$ (s)	Filter	Magnitude ^a	1σ Error
PAIRITEL			
11677	<i>H</i>	15.772	0.139
12004	<i>H</i>	15.812	0.145
12333	<i>H</i>	15.767	0.139
12897	<i>H</i>	15.872	0.097
13695	<i>H</i>	15.812	0.095
14513	<i>H</i>	16.162	0.127
15332	<i>H</i>	16.013	0.107
16170	<i>H</i>	16.306	0.138
16969	<i>H</i>	16.228	0.129
18407	<i>H</i>	16.340	0.095
20464	<i>H</i>	16.363	0.096
22523	<i>H</i>	16.644	0.112
24580	<i>H</i>	16.800	0.135
28290	<i>H</i>	17.093	0.138
31929	<i>H</i>	17.225	0.277
36517	<i>H</i>	17.723	0.258

^aPAIRITEL Magnitude are in Vega system.

TABLE 14
PHOTOMETRIC OBSERVATIONS FOR GRB 110205A

$T - T_0$ (s)	Filter	Magnitude ^a	1σ Error
PAIRITEL			
11677	<i>K</i>	15.127	0.183
12004	<i>K</i>	15.228	0.205
12333	<i>K</i>	14.816	0.143
12897	<i>K</i>	15.345	0.149
13695	<i>K</i>	15.224	0.132
14513	<i>K</i>	15.352	0.152
15332	<i>K</i>	15.360	0.142
16170	<i>K</i>	15.480	0.161
16969	<i>K</i>	15.359	0.146
18407	<i>K</i>	15.478	0.107
20464	<i>K</i>	15.772	0.140
22523	<i>K</i>	15.967	0.155
24580	<i>K</i>	16.103	0.178
28290	<i>K</i>	16.255	0.140
31929	<i>K</i>	16.586	0.300
36517	<i>K</i>	16.782	0.210

^aPAIRITEL Magnitude are in Vega system.

TABLE 15
PHOTOMETRIC OBSERVATIONS FOR GRB 110213A

$T - T_0$ (s)	Filter	Magnitude ^a	1σ Error
<i>Swift</i> -UVOT			
322	<i>u</i>	15.27	0.07
342	<i>u</i>	15.44	0.08
362	<i>u</i>	15.59	0.09
382	<i>u</i>	15.66	0.09
402	<i>u</i>	15.52	0.08
422	<i>u</i>	15.55	0.08
437	<i>u</i>	15.58	0.03
442	<i>u</i>	15.62	0.09
462	<i>u</i>	15.65	0.09
482	<i>u</i>	15.60	0.08
502	<i>u</i>	15.60	0.09
522	<i>u</i>	15.67	0.09
542	<i>u</i>	15.65	0.09
562	<i>u</i>	15.76	0.13
722	<i>u</i>	15.93	0.11
726	<i>u</i>	15.96	0.10
742	<i>u</i>	16.07	0.25
1130	<i>u</i>	16.53	0.13
1305	<i>u</i>	16.43	0.12
1478	<i>u</i>	16.85	0.15
1651	<i>u</i>	16.65	0.14
1825	<i>u</i>	16.42	0.12
1998	<i>u</i>	16.62	0.14
2171	<i>u</i>	16.69	0.14
2346	<i>u</i>	16.54	0.13
2519	<i>u</i>	16.51	0.13
5960	<i>u</i>	16.53	0.05
7397	<i>u</i>	16.81	0.05
12699	<i>u</i>	17.34	0.06
13002	<i>u</i>	17.39	0.06
13306	<i>u</i>	17.50	0.06
19468	<i>u</i>	18.42	0.11
19771	<i>u</i>	18.37	0.11
19973	<i>u</i>	18.44	0.21
30140	<i>u</i>	19.22	0.22
30443	<i>u</i>	19.33	0.23
30747	<i>u</i>	19.06	0.19
37052	<i>u</i>	19.26	0.23
37282	<i>u</i>	19.28	0.32
48340	<i>u</i>	19.68	0.32
48856	<i>u</i>	19.20	0.33
182877	<i>u</i>	> 20.87	

^aUVOT magnitude are in the natural UVOT photometric system (Vega). See Breeveld et al. (2011) for the most updated zeropoint and conversion factors.

TABLE 16
PHOTOMETRIC OBSERVATIONS FOR GRB 110213A

$T - T_0$ (s)	Filter	Magnitude ^a	1σ Error
<i>Swift</i> -UVOT			
577	<i>b</i>	16.07	0.08
751	<i>b</i>	16.49	0.10
1155	<i>b</i>	16.70	0.10
1330	<i>b</i>	16.89	0.11
1502	<i>b</i>	16.99	0.12
1675	<i>b</i>	17.03	0.13
1850	<i>b</i>	17.12	0.14
2023	<i>b</i>	17.23	0.14
2196	<i>b</i>	17.24	0.15
2371	<i>b</i>	16.95	0.12
2544	<i>b</i>	17.22	0.15
6167	<i>b</i>	16.86	0.04
7603	<i>b</i>	17.16	0.04
13611	<i>b</i>	17.86	0.06
13915	<i>b</i>	17.86	0.06
14155	<i>b</i>	18.03	0.08
31052	<i>b</i>	19.58	0.22
431692	<i>b</i>	> 20.91	0.22

^aUVOT magnitude are in the natural UVOT photometric system (Vega). See Breeveld et al. (2011) for the most updated zeropoint and conversion factors.

TABLE 17
PHOTOMETRIC OBSERVATIONS FOR GRB 110213A

$T - T_0$ (s)	Filter	Magnitude ^a	1σ Error
<i>Swift</i> -UVOT			
652	<i>v</i>	15.66	0.11
825	<i>v</i>	16.09	0.14
1056	<i>v</i>	16.15	0.15
1231	<i>v</i>	15.99	0.13
1404	<i>v</i>	15.90	0.12
1577	<i>v</i>	16.36	0.16
1751	<i>v</i>	16.27	0.15
1925	<i>v</i>	16.40	0.18
2098	<i>v</i>	16.64	0.20
2272	<i>v</i>	16.85	0.23
2445	<i>v</i>	16.32	0.15
2618	<i>v</i>	16.46	0.17
6782	<i>v</i>	16.32	0.05
8218	<i>v</i>	16.55	0.06
24339	<i>v</i>	18.48	0.20
24644	<i>v</i>	18.64	0.22
24948	<i>v</i>	18.29	0.16
42061	<i>v</i>	19.18	0.36
451502	<i>v</i>	> 20.66	

^aUVOT magnitude are in the natural UVOT photometric system (Vega). See Breeveld et al. (2011) for the most updated zeropoint and conversion factors.

TABLE 18
PHOTOMETRIC OBSERVATIONS FOR GRB 110213A

$T - T_0$ (s)	Filter	Magnitude ^a	1σ Error
<i>Swift</i> -UVOT			
104	<i>white</i>	17.33	0.20
112	<i>white</i>	17.12	0.18
120	<i>white</i>	17.51	0.23
128	<i>white</i>	16.76	0.13
136	<i>white</i>	16.67	0.13
144	<i>white</i>	16.62	0.12
152	<i>white</i>	16.07	0.09
160	<i>white</i>	16.42	0.11
168	<i>white</i>	16.19	0.09
176	<i>white</i>	16.04	0.08
184	<i>white</i>	16.30	0.10
192	<i>white</i>	16.01	0.08
200	<i>white</i>	16.08	0.09
208	<i>white</i>	16.03	0.08
216	<i>white</i>	15.93	0.08
224	<i>white</i>	15.99	0.08
232	<i>white</i>	15.98	0.08
240	<i>white</i>	15.83	0.07
248	<i>white</i>	15.83	0.09
592	<i>white</i>	16.02	0.10
600	<i>white</i>	16.17	0.08
602	<i>white</i>	16.09	0.05
608	<i>white</i>	16.03	0.07
768	<i>white</i>	16.44	0.10
775	<i>white</i>	16.33	0.05
776	<i>white</i>	16.35	0.08
784	<i>white</i>	16.15	0.09
941	<i>white</i>	16.45	0.02
1176	<i>white</i>	16.69	0.10
1179	<i>white</i>	16.63	0.06
1184	<i>white</i>	16.55	0.09
1352	<i>white</i>	16.70	0.10
1354	<i>white</i>	16.74	0.06
1360	<i>white</i>	16.81	0.10
1520	<i>white</i>	16.73	0.10
1527	<i>white</i>	16.83	0.07
1528	<i>white</i>	16.77	0.10
1536	<i>white</i>	17.04	0.15
1695	<i>white</i>	16.84	0.09
1705	<i>white</i>	16.84	0.09
1865	<i>white</i>	17.02	0.15
1875	<i>white</i>	16.87	0.09
1885	<i>white</i>	17.54	0.22
2035	<i>white</i>	16.59	0.17
2045	<i>white</i>	16.95	0.10
2055	<i>white</i>	16.98	0.12
2215	<i>white</i>	16.87	0.10
2225	<i>white</i>	16.84	0.09
2385	<i>white</i>	16.92	0.14
2395	<i>white</i>	16.94	0.10
2405	<i>white</i>	16.89	0.14

TABLE 18—*Continued*

$T - T_0$ (s)	Filter	Magnitude ^a	1σ Error
2555	<i>white</i>	17.18	0.30
2565	<i>white</i>	16.97	0.10
2575	<i>white</i>	16.78	0.10
6371	<i>white</i>	16.83	0.03
7807	<i>white</i>	17.04	0.03
183368	<i>white</i>	21.57	0.31

^aUVOT magnitude are in the natural UVOT photometric system (Vega). See Breeveld et al. (2011) for the most updated zeropoint and conversion factors.

TABLE 19
PHOTOMETRIC OBSERVATIONS FOR GRB 110213A

$T - T_0$ (s)	Filter	Magnitude (AB)	1σ Error
KAIT			
74	<i>clear</i>	17.34	0.10
77	<i>clear</i>	17.03	0.08
81	<i>clear</i>	17.05	0.08
84	<i>clear</i>	16.91	0.07
87	<i>clear</i>	16.88	0.06
90	<i>clear</i>	16.68	0.06
93	<i>clear</i>	16.56	0.05
97	<i>clear</i>	16.59	0.05
100	<i>clear</i>	16.47	0.05
103	<i>clear</i>	16.37	0.05
195	<i>clear</i>	15.07	0.01
295	<i>clear</i>	14.96	0.01
395	<i>clear</i>	15.04	0.01
495	<i>clear</i>	15.22	0.01
595	<i>clear</i>	15.34	0.01
695	<i>clear</i>	15.47	0.01
795	<i>clear</i>	15.57	0.01
894	<i>clear</i>	15.67	0.01
992	<i>clear</i>	15.75	0.01
1092	<i>clear</i>	15.84	0.01
1192	<i>clear</i>	15.90	0.01
1290	<i>clear</i>	15.97	0.01
1390	<i>clear</i>	16.03	0.01
1488	<i>clear</i>	16.07	0.01
1588	<i>clear</i>	16.12	0.01
1655	<i>clear</i>	16.13	0.01
1722	<i>clear</i>	16.15	0.01
1788	<i>clear</i>	16.19	0.01
1853	<i>clear</i>	16.21	0.01
1920	<i>clear</i>	16.25	0.01
1986	<i>clear</i>	16.27	0.01
2053	<i>clear</i>	16.33	0.01
2120	<i>clear</i>	16.27	0.01
2186	<i>clear</i>	16.24	0.01
2253	<i>clear</i>	16.26	0.01
2320	<i>clear</i>	16.27	0.01
2386	<i>clear</i>	16.14	0.01
2454	<i>clear</i>	16.12	0.01
2518	<i>clear</i>	16.16	0.01
2585	<i>clear</i>	16.13	0.01
78843	<i>clear</i>	19.85	0.10
84641	<i>clear</i>	20.22	0.10
86515	<i>clear</i>	20.14	0.15

TABLE 20
PHOTOMETRIC OBSERVATIONS FOR GRB 110213A

$T - T_0$ (s)	Filter	Magnitude	1σ Error
Palomar telescope			
2304	g'	16.449	0.009
2892	g'	16.364	0.005
3480	g'	16.260	0.006
3775	g'	16.359	0.007
4343	g'	16.195	0.007
4900	g'	16.072	0.005
5463	g'	16.184	0.006
6026	g'	16.190	0.006
6579	g'	16.296	0.006
88212	g'	20.669	0.155

TABLE 21
PHOTOMETRIC OBSERVATIONS FOR GRB 110213A

$T - T_0$ (s)	Filter (AB)	Magnitude	1σ Error
KAIT			
128	V	15.81	0.03
228	V	15.13	0.02
328	V	15.14	0.02
428	V	15.24	0.02
528	V	15.36	0.02
628	V	15.55	0.02
728	V	15.67	0.03
828	V	15.675	0.03
926	V	15.84	0.03
1026	V	15.93	0.03
1126	V	15.97	0.03
1226	V	16.05	0.03
1324	V	16.08	0.03
1422	V	16.13	0.03
1522	V	16.19	0.03

TABLE 22
 PHOTOMETRIC OBSERVATIONS FOR GRB 110213A

$T - T_0$ (s)	Filter	Magnitude	1σ Error
Palomar Telescope			
162	r'	15.326	0.006
248	r'	14.956	0.005
582	r'	15.271	0.005
839	r'	15.584	0.003
1131	r'	15.853	0.018
1247	r'	15.912	0.005
1575	r'	16.094	0.006
1862	r'	16.198	0.005
2450	r'	16.103	0.005
3038	r'	16.121	0.005
3632	r'	15.976	0.006
4205	r'	15.974	0.005
4762	r'	15.802	0.005
5315	r'	15.804	0.005
5888	r'	15.886	0.005
6441	r'	15.937	0.006
6994	r'	16.083	0.006
88628	r'	20.303	0.083
Gemini-N Telescope			
526800	r'	24.27	0.13

TABLE 23
PHOTOMETRIC OBSERVATIONS FOR GRB 110213A

$T - T_0$ (s)	Filter	Magnitude (AB)	1σ Error
KAIT telescope			
161	<i>I</i>	14.64	0.02
261	<i>I</i>	14.37	0.02
361	<i>I</i>	14.41	0.02
461	<i>I</i>	14.60	0.02
561	<i>I</i>	14.74	0.02
661	<i>I</i>	14.84	0.02
761	<i>I</i>	14.97	0.02
861	<i>I</i>	15.05	0.02
959	<i>I</i>	15.16	0.02
1059	<i>I</i>	15.24	0.02
1159	<i>I</i>	15.32	0.02
1257	<i>I</i>	15.39	0.02
1357	<i>I</i>	15.42	0.02
1455	<i>I</i>	15.51	0.02
1555	<i>I</i>	15.54	0.03
1622	<i>I</i>	15.56	0.03
1688	<i>I</i>	15.63	0.03
1755	<i>I</i>	15.64	0.03
1822	<i>I</i>	15.63	0.03
1886	<i>I</i>	15.64	0.03
1953	<i>I</i>	15.68	0.03
2020	<i>I</i>	15.72	0.03
2086	<i>I</i>	15.76	0.03
2153	<i>I</i>	15.69	0.03
2220	<i>I</i>	15.64	0.03
2287	<i>I</i>	15.67	0.03
2353	<i>I</i>	15.63	0.03
2420	<i>I</i>	15.58	0.03
2485	<i>I</i>	15.57	0.03
2551	<i>I</i>	15.54	0.03
2618	<i>I</i>	15.53	0.03
Palomar telescope			
334	<i>i'</i>	14.322	0.006
667	<i>i'</i>	14.843	0.005
924	<i>i'</i>	15.103	0.005
1343	<i>i'</i>	15.407	0.005
1661	<i>i'</i>	15.573	0.005
2013	<i>i'</i>	15.673	0.003
2601	<i>i'</i>	15.528	0.005
3183	<i>i'</i>	15.550	0.003
3913	<i>i'</i>	15.439	0.006
4481	<i>i'</i>	15.183	0.003
5039	<i>i'</i>	15.124	0.005
5601	<i>i'</i>	15.265	0.005
6164	<i>i'</i>	15.258	0.005
6717	<i>i'</i>	15.414	0.006
89048	<i>i'</i>	19.611	0.054
262255	<i>i'</i>	22.315	0.371
Gemini telescope			

TABLE 23—*Continued*

$T - T_0$ (s)	Filter	Magnitude (AB)	1σ Error
526800	i'	23.68	0.09

TABLE 24
PHOTOMETRIC OBSERVATIONS FOR GRB 110213A

$T - T_0$ (s)	Filter	Magnitude	1σ Error
Palomar telescope			
419	z'	13.910	0.004
753	z'	14.383	0.006
1010	z'	14.630	0.007
1433	z'	14.928	0.010
1747	z'	15.076	0.011
2159	z'	15.121	0.008
2746	z'	14.877	0.007
3334	z'	14.793	0.006
4056	z'	14.843	0.006
4624	z'	14.679	0.005
5177	z'	14.604	0.005
5744	z'	14.721	0.006
6302	z'	14.762	0.006
6855	z'	14.929	0.006